Chapter 15
Modeling and Control of a Wind Turbine

R. Tapia Sánchez and A. Medina Rios

Abbreviations

DFIG	Doubly fed induction generator
MSC	Machine side converter
NSC	Network side converter
DC	Direct current
Cp	Power coefficient
BEM	Blade element momentum
DFIM	Doubly fed induction motor

15.1 Introduction

Wind turbine is a complex system in which different technical areas are involved. Some publications deal with this topic, e.g., [22, 24, 25]. In [22] a parametric and nonparametric model is proposed using advantage algorithms, only the power curve is considered. Other contribution [25] reviews recent research of numerical simulation applied to wind energy and in [24] the modeling of a small-scale distributed power system containing the power demand, a wind turbine, the photovoltaic arrays, and the electrical connection is presented. These contributions highlight the importance of having a reliable model of the wind turbine, in order to conduct dynamic studies of such system. Nevertheless, the use of different techniques previously developed, and the complexity of a wind turbine make

R.T. Sánchez (✉) • A.M. Rios
División de Estudios de Posgrado, Facultad de Ingeniería Eléctrica, Universidad Michoacana de San Nicolás de Hidalgo, Morelia 58000, Mexico
e-mail: rtsanchez@dep.fie.umich.mx

© Springer International Publishing Switzerland 2017

W. Borutzky (ed.), *Bond Graphs for Modelling, Control and Fault Diagnosis of Engineering Systems*, DOI 10.1007/978-3-319-47434-2_15

possible to visualize even different approaches for their study and analysis. Under this context, in order to analyze the system in the same reference frame, the bond graph methodology [3, 19, 37] can represent the whole structure. This methodology presents some properties that can be applied directly to the model [7].

The bond graph wind turbine model has been addressed in several works, e.g., [1, 10, 46]. In the first publication, a detailed model of a blade is proposed. The aerodynamic structural forces are considered, and also real data of a wind turbine are used, in order to calculate the output torque. Besides, it is a general model that can be applied to any wind turbine blade. In [46] a six-mass drive train model is presented. This complete model is formulated and then simplified. The authors did not use real parameters of a wind turbine and the aerodynamics forces are not considered. In [10], a complete wind turbine based on parameters taken from a real turbine is proposed. The model presents all components of the wind turbine, but the aerodynamics are not considered in detail. The publication is centered on drive train effects.

The mechanical part of the wind turbine presented in this chapter is taken from [44] which consider the blade model presented in [1].

Nowadays, most of the installed wind turbines have kept the configuration with the use of a gearbox. Based on this context, a model of the gearbox is used in order to complete the whole system. In terms of a bond graph methodology, gears have been modeled for transmission applications [6, 8]. The model used here is based on the one reported in [21], in which a planetary gears is adopted. Also, in [17] a complete review of graphical tools for modeling gears is given. The authors conclude that bond graph methodology has major properties, when compared to others. It is important to mention that gearbox is the most important part of a wind turbine, because is at this stage where most of faults occur. It is estimated that a wind turbine has around 20 years of life span, but normally the gearbox needs to be replaced every 5 years [36].

In this chapter a complete bond graph model of a variable-speed wind turbine with doubly fed induction generator (DFIG) configuration is presented, which accounts real data and parameters of a real wind turbine of 750 kW [13]. This configuration has some important advantages, e.g., the possibility of controlling active and reactive power, the capability of reducing stresses of the mechanical structure, and acoustic noise [5]. Also, losses in the power electronics converter are reduced, as compared to a direct-driver synchronous/induction generator (variable-speed wind turbine with induction generator configuration). This is due to the fact that the converter placed between the grid and the double-fed induction machine rotor handles only a fraction of the turbine rate power [26, 47].

The control of a DFIG has been addressed in several works, e.g., [9, 15, 32, 35]. In [9] a sliding mode control is used, and in [35] the power control of a doubly fed induction machine via output feedback is presented. The behavior of such machines in large wind farms, along with the general active and reactive power control has been addressed in [15]. A novel simplified model of the DFIG appropriate for bulk power system studies is presented in [32]. In this chapter, the control law developed

in [45] is taken because this control presents a different structure and the bond graph model of the DFIG is used in order to obtain the control law applying the bicausality concepts [11].

The outline of this chapter is as follows: the model description is given in Sect. 15.2. Then, the wind turbine model is detailed in Sect. 15.3. The DFIG control is described in Sect. 15.4. The whole system is simulated in Sect. 15.5. The global conclusions of the chapter are drawn in Sect. 15.6.

15.2 System Description

The wind turbine connected to the electrical network can be represented by Fig. 15.1. Every single part (blades, hub, bearings, brake, and hub) of the wind turbine scheme is joined by a bond. In most of the elements there is an associated mechanical power, but the last part (DFIG) transforms this mechanical power into a three phase electrical power, represented by three bonds. The stator is directly connected to the power network, while the rotor is connected through slip rings to a power electronic converter.

Different considerations can be made for the study of this system. Here, an analysis of the complete model is presented, by considering all the components as shown in Fig. 15.1.

The function of blades is to convert the wind velocity into a torque, transforming the wind into a force and then into a torque. In Fig. 15.1, the causality of the first bond shows that torque is provided by the blades.

A large torque is produced by blades, and is transferred to the gearbox, which transforms this big torque into a small one, to be applied into generator. A similar situation is valid for angular velocity, i.e., there is a high speed provided for generator, which is transformed by the gearbox into a low speed, presented in the rotor turbine (hub).

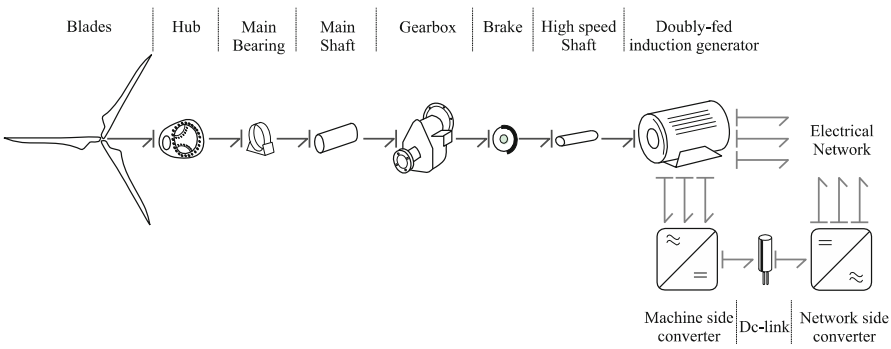

Fig. 15.1 Wind turbine presented in terms of word bond graph

From the generator point of view, a wind turbine has different configurations. Also, the wind turbine can operate with either under fixed-speed or variable-speed mode. This operation depends directly on the generator connection. It means that for fixed-speed wind turbines, the generator is directly connected to the power network, since the speed is closely tied to the grid frequency. Besides, for a variable-speed wind turbine, the generator is controlled through power electronics converters, which make possible to control the rotor speed. Therefore, as it was mentioned before, a variable-speed wind turbine with doubly fed generator configuration is used (Fig. 15.1).

The main advantage of this configuration is the fact that the power electronic converter has to handle only a fraction (30 %) of the total power [47]. Therefore, the losses in the power electronic converter can be reduced.

Two power electronics converters: machine side converter (MSC) and network side converter (NSC) are used in order to have a DC-link between them, thus allowing the power transfer. With the MSC, it is possible to control the torque or speed in the DFIG and the power factor at the stator terminals, while with the NSC functions the DC-link voltage is kept constant.

In the following sections the model of each elements is presented.

15.3 Model Components

In this section the individual bond graph models for the blades, the gearbox, the doubly fed induction generator, and the converters are presented.

15.3.1 Blades

As mentioned before, the blade model is taken from [1]. In that publication, the blade structure represents a general model; it means that wind turbines of different powers capacity can be simulated by changing the data. The model presented in [1] is divided into three sections; however, it can be divided into more sections. Here this model is recalled, since it represents the blade aerodynamic wind turbine. Nevertheless, the blade is divided into only two sections to allow the improvement of results, in terms of the coefficient of power Cp, as it will be later shown in this section.

There are problems in system modeling, where lumping of inertia and compliance, used in rigid body dynamics, fails to get the essential dynamics of the system. Situations like this often arise with systems consisting of long slender members, whose flexibility plays an important role in the dynamics of the system. For example, in wind turbine modeling, it will be inadequate to treat the blade as a rigid body. These members are essentially distributed system parameters, governed by partial differential equations, and are lumped in space by finite approximation.

The model is based on Rayleigh Beam Model [29] and the Blade Element Momentum (BEM) theory [16]; it is a dynamic model in which a modal analysis can be made. Then, the blade *is formed by* two main parts: the structural and the aerodynamic.

15.3.1.1 Model Structure

The structure of the blade is made using C-field and R-field elements, which represent the stiffness and the structural damping matrix between the center of gravity of adjacent elements, respectively. These matrices are calculated at the center of gravity of adjacent elements. Figure 15.2a shows a schematic of a cantilever beam with regulation and lumping of inertia, which is used in the bond graph formulation.

As it is shown, the whole blade structure is divided into two sections. The length of each section is the same, 11.7 m, thus allowing a blade of 23.4 m, which is the characteristic blades length for a 750 kW wind turbine.

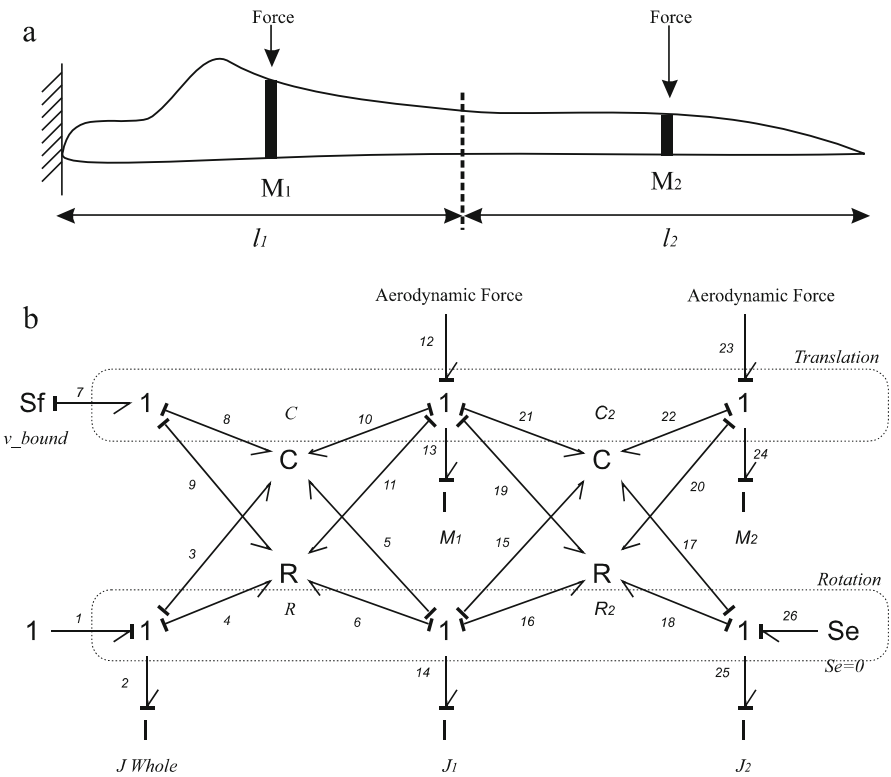

Fig. 15.2 (**a**) Cantilever beam of blade and (**b**) structural bond graph of blade

The bond graph model presented in Fig. 15.2b shows the translation and rotation motion at the top and bottom of the figure, respectively. Aerodynamic forces for each section are applied in the translation structure (bonds 12 and 23); this means that the effort is imposed.

The stiffness matrix is modeled as a 4–port C–field storing, due to the four generalized displacements shown in Fig. 15.2b. In terms of flexural rigidity (EI) and element length (l), the stiffness matrix is given by Eq. (15.1).

$$[K_i] = \frac{EI}{l^3}\begin{bmatrix} 12 & 6l & -12 & 6l \\ 6l & 4l^2 & -6l & 2l^2 \\ -12 & -6l & 12 & -6l \\ 6l & 2l^2 & -6l & 4l^2 \end{bmatrix} \tag{15.1}$$

where E is the Young module of the material, and I the second moment of area about the axis of deflection. The structural damping matrix is given by $[R_i] = \mu[K_i]$, where the μ factor represents the coefficient of structural damping.

The boundary condition of the model is represented by the Sf:v_bound and Se sources. The connection between the blade and the hub is assumed to be rigid, i.e., Sf:v_bound = 0, and the blade has only one degree of freedom Se = 0. Finally, the rotating inertia J_whole is the rigid body inertia of the whole blade.

Dynamic equations and also the natural frequencies of the blade can be directly obtained from the bond graph of Fig. 15.2b. In this case, the main dynamics around the blade structure take into account the parameters (given in Appendix (Table 15.6)) for an NACA 4415 blade [48].

Considering Fig. 15.2b the causal loops and causal paths are presented in Table 15.1. The causal loops consider the **C** and **R** matrix values, in order to calculate the frequency. Therefore, each causal loop involved with one I element and one element of the damping matrix (**R**) is considered. Besides, there are causal paths present in the model, between the I-elements and the stiffness matrix, and Table 15.1 shows also the numerical values of these causal paths. It is important to mention that the main frequencies are produced only by the causal loops.

As shown in Table 15.1, the loop involving the translational mass M_1 of section 1 has small values (bonds 11, 13, 19), compared to the mass M_2 (bonds 20, 24). This verified that high frequency vibrations are introduced by the last blade sections, and

Table 15.1 Causal loop and causal paths frequencies

Causal loop	2 → 4 → 4 → 2	14 → 6 → 6 → 14	14 → 16 → 16 → 14	25 → 18 → 18 → 25	13 → 11 → 11 → 13	13 → 19 → 19 → 13	24 → 20 → 20 → 24
Frequency (rad/s)	120.88	36632.9	54245	76827.7	8.77	12.99	32.22
Causal path	2 → 3	14 → 5	13 → 10	14 → 15	13 → 21	25 → 17	24 → 22
Frequency (rad/s)	690832.9	39685.3	224807.7	39685.33	224807.8	9873.15	482100.3

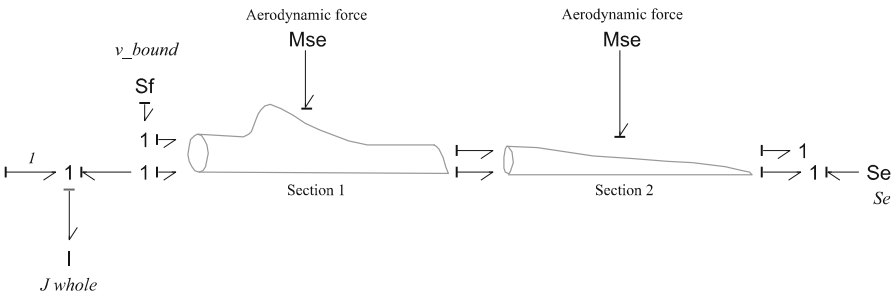

Fig. 15.3 Two sections (sub-model) bond graph blade

low frequencies are presented in the first blade section (it is the same for the inertias J_1 and J_2). A similar behavior is presented for the causal paths; the high frequency is introduced by the last blade sections. It is important to say that these are not the real natural frequencies, they are only an approximation. If an exactly value is required, then a matrix structure needs to be found, taking into account all the causal loops and path of the whole structure.

The model of the blade can be represented by sub-models, as shown in Fig. 15.3. The rotating inertia J whole presents a derivative causality because the angular velocity is given by bond 1. This means that the blade gives the torque as output and then it needs the angular velocity as input. Besides, bond 1 makes it possible to have a connection with the hub.

The two modulate sources of effort, which represent the aerodynamic force, need to be calculated from the input wind. This means that the wind speed needs to be converted into aerodynamical force. This process will be presented in the next subsection.

15.3.1.2 Aerodynamic Force

The aerodynamic loading is caused by the flow (wind) past the structure, in other words the blades and the tower. Accurate models of the aerodynamic aspects of wind turbines are essential to successfully design and analyze wind energy systems. Wind turbine aerodynamic models are used to relate wind inflow conditions to loads applied to the turbine.

The subsequent analysis develops the most common aerodynamics theory employed in the wind turbine design and analysis environment. It consists on the blade element momentum theory (BEM), the fundamental aerodynamic theory used by the bond graph model presented in this paper.

The whole BEM theory can be found in [27]. Here, the used mathematical expressions will be recalled, as well as the principal expressions taken from [1], which are necessary to convert the wind into an aerodynamic force.

As it was explained before, blade structure is divided into sections. For each section BEM theory is applied, in order to provide aerodynamic force to the blade structure. Equation (15.2) expresses the aerodynamic force F_i applied to the ith section.

$$F_i = \left(\frac{1}{2} \rho V_w \frac{(1 - a_i)^2}{\sin^2 \varphi_i} \left(C_{li} \sin \varphi_i - C_{di} \cos \varphi_i \right) c_i l_i \right) V_w \tag{15.2}$$

where V_w represents the wind velocity, ρ the air density, φ_i the wind inflow angle (Eq. (15.3)), C_{li} and C_{di} are the lift and drag dimensionless coefficients function on the angle of attack α_i, defined as the angle between the incoming flow stream and the chord line of the airfoil in the ith section. Also, a_i represents the axial tangential induction factor and is calculated from Eqs. (15.4) and (15.5).

$$\varphi_i = \tan^{-1} \left(\frac{V_w (1 - a_i)}{\Omega_r r_i (1 + a_i')} \right) \tag{15.3}$$

$$a_i = \left(1 + \frac{4 \sin^2 \varphi_i}{\sigma_i' \left(C_{li} \cos \varphi_i + C_{di} \sin \varphi_i \right)} \right)^{-1} \tag{15.4}$$

$$a_i' = \left(-1 + \frac{4 \sin^2 \varphi_i}{\sigma_i' \left(C_{li} \cos \varphi_i - C_{di} \sin \varphi_i \right)} \right)^{-1} \tag{15.5}$$

Parameters involving in last expressions are graphically represented in Fig. 15.4.

A modulated gyrator MGY element is used to implement Eqs. (15.2), (15.3), (15.4), and (15.5), since wind is transformed into an aerodynamic force, as shown in Fig. 15.5.

Modulated inputs to MGY elements of Fig. 15.5 are the pitch angle and the angular velocity Ωr.

In order to simulate the blade model, Eqs. (15.2), (15.3), (15.4), and (15.5) are placed within each MGY element; it means that their traditionally constitutive relation is changed. These expressions represent an iterative process, where the axial tangential induction factor and the wind inflow angle are changed. The code

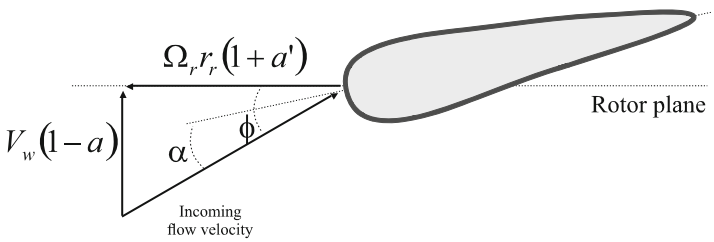

Fig. 15.4 Velocities at rotor blade

Fig. 15.5 Representation of aerodynamic force conversion

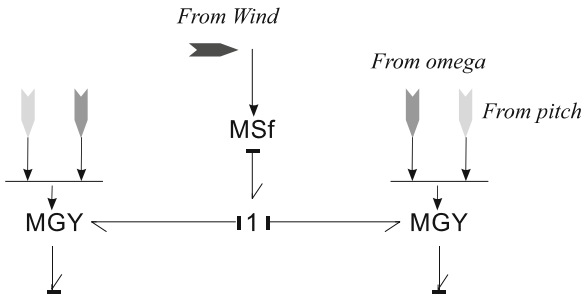

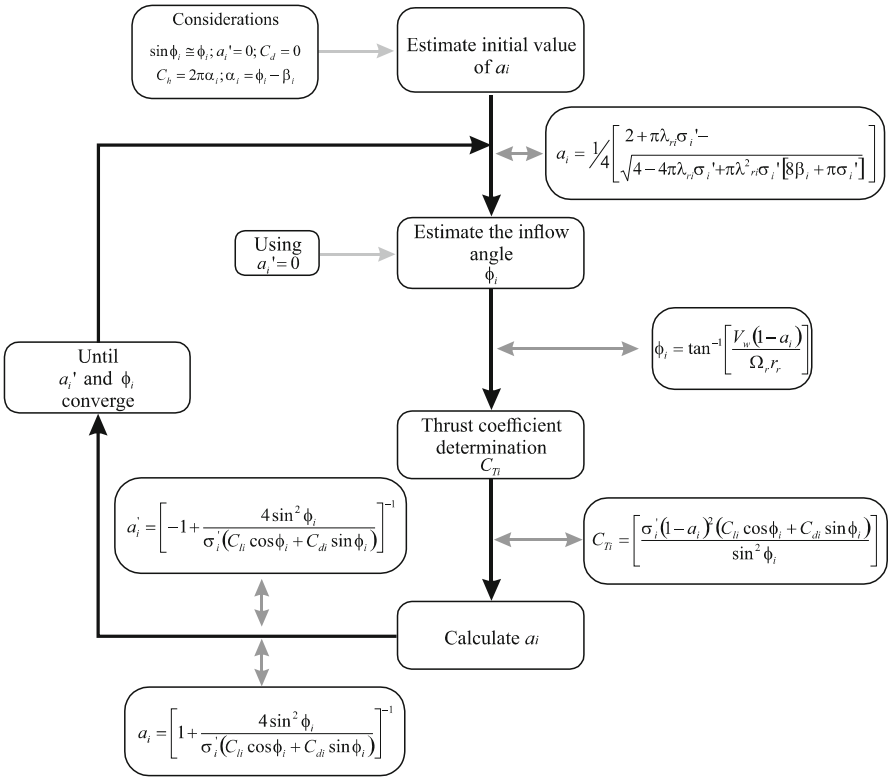

Fig. 15.6 Flow diagram code

flow diagram is shown in Fig. 15.6. In order to estimate the initial value of the axial induction factor, some conditions are assumed at the starting time; then, an estimation of the inflow angle is made. This allows to determinate the accurate coefficient [4]. After that, the calculation of the axial and tangential induction factor is performed and the new value is used for the next cycle. This iterative process is conducted until the tangential induction factor and wind inflow angle have converged to their final values.

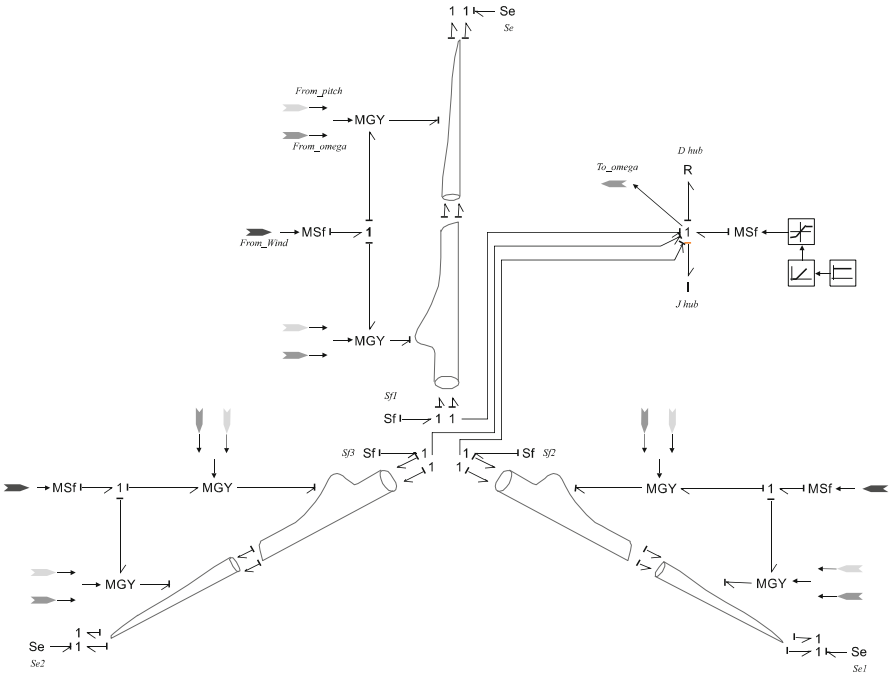

Fig. 15.7 Three blades and hub model

Figure 15.6 also shows the mathematical expressions involved in each stage.

It is important to observe that, due to the complexity involving in the aerodynamic force conversion, the use of the MGY element was necessary. Nevertheless, it can be possible to model this part in terms of bond graph allowing having a physical behavior of this conversion.

A simulation is carried out in order to verify the dynamic response of blades; this is made using the 20Sim software (www.20sim.com). Figure 15.7 shows the simulation scheme.

Three blades are used; each of them is divided into two sections with the forces from the wind in each section applied. The rotating inertia J_{hub} corresponds to the hub structure and represents the rotating inertia of each blade and the hub itself; it means that $J_{\text{hub}} = 3{*}J_{\text{whole}} + J_{\text{hub}}$ itself. Besides, the R element called D_{hub} represents the main bearing.

To observe the transient response in the modulated flow source MSf the angular velocity applied with a ramp profile is used. The traditional curve of power coefficient versus tip speed (Cp vs λ) is shown in Fig. 15.8.

In Fig. 15.8, the maximum Cp obtained is 0.4, having a tip speed of 7.4; the theoretical maximum value of Cp is 0.59 (due to Betz limit), at around a tip speed of 8. In practical designs, the maximum achievable Cp is below 0.5 for high speed, two-blade turbines, and between 0.2 and 0.4 for slow speed turbines with more

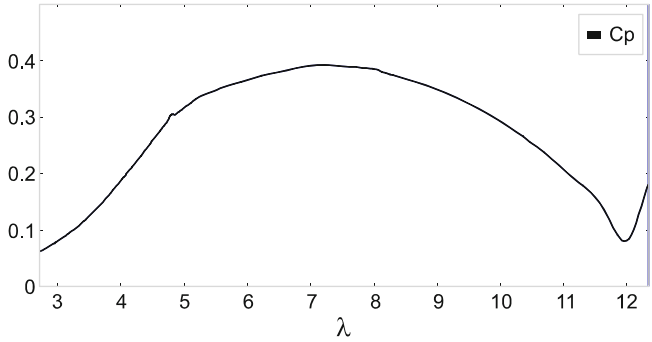

Fig. 15.8 Curve of Cp vs λ

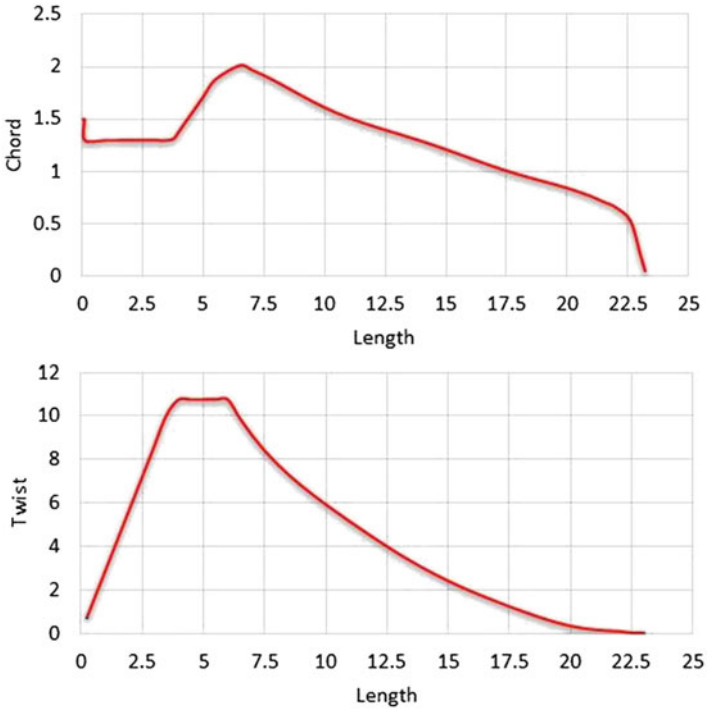

Fig. 15.9 Chord and twist along the blade

blades [33]. The approximation to standard values is acceptable and it is better that the value shown in [1] (around 0.33). The improvement results from taking two sections of the blade allow applying the aerodynamic force with maximum chore and twisting distribution (Fig. 15.9) along the blade length.

Figure 15.9 shows the chord and twist along the blade. By the action of twisting, the wind comes with a large angle of incidence as it approaches the bottom of blade.

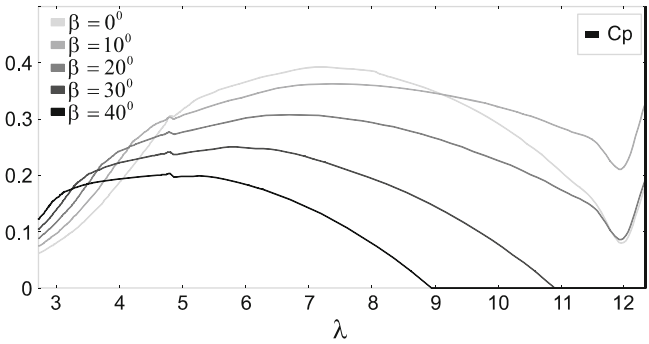

Fig. 15.10 Curve Cp vs λ for different pitch angles

Then, the chord is the distance between the leading edge and the trailing edge of the blade section. According to these two figures, the values of chore and twist taken for each section are presented in the Appendix.

It is known that pitch angle is another important parameter in wind turbines, since the power generated by the turbine needs to be regulated with this parameter. Figure 15.10 shows the Cp coefficient for different pitch angle values, and confirms that dynamical model of the blade + hub + main bearing adequately performs. This is because when the pitch angle increases, the mechanical power decreases.

15.3.2 Gearbox

A planetary stage and two more parallel stages (to increase the angular velocity) normally compose the gearbox of a wind turbine. Figure 15.11 shows the gearbox scheme.

Bond graph models of gears have been addressed in previous contributions [6, 8]. The simplest way to model the gearbox is as a whole structure; it means that conversion ratio (N_p/N_g, where N_p is the teeth number of pinion and N_g the teeth number of gears) can be introduced directly in a transformer element TF. However, as the gearbox is one of the most important parts of a wind turbine due to its involved dynamics; thus, a more precise model needs to be developed.

In [17, 21] a detailed gearbox bond graph model is proposed. In [17] the authors detail the technique, making a comparison of different methodologies in a gear analysis, and in [21] a planetary gear system is presented. The last publication is taken as a reference for the wind turbine gearbox model.

Then, in the gearbox model some considerations are taken into account, i.e.,

- Ring gear is a fixed stage.
- Only one parallel stage is considered (including the two parallel stage effects).
- Carrier is considered as input; however, sun is the output.

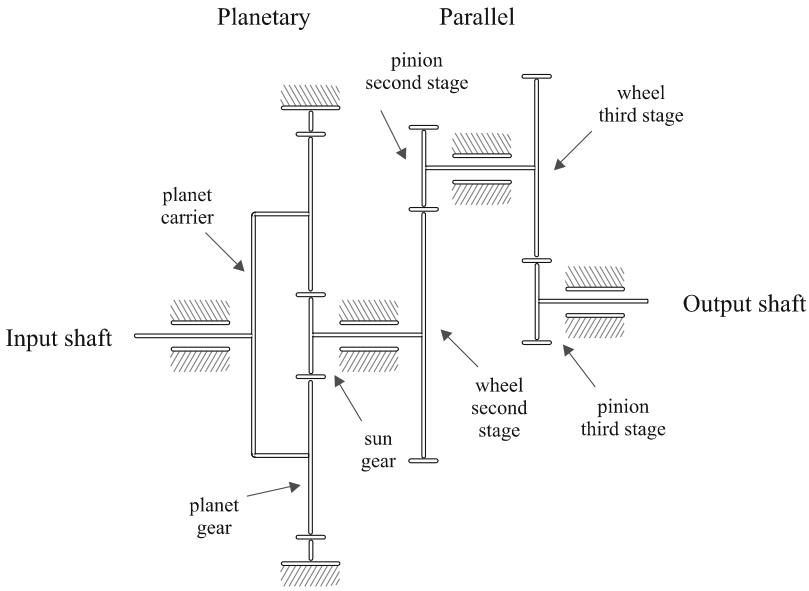

Fig. 15.11 Gearbox schema

– Mesh stiffness between planet-ring and planet-sun is considered.
– Bearing stiffness are not considered in the model.

15.3.2.1 Analysis of the Gearbox Model

The bond graph model formulation is made taking as a reference (Fig. 15.11), and the consideration above mentioned. Figure 15.12 shows the gearbox bond graph model.

The model of Fig. 15.12 shows the three planet gears represented by momentum of inertias J_{pj} ($j = 1, 2, 3$). These planets are bounded to sun and ring gears by the mesh stiffness K_{sp} and K_{rp}, respectively. Also, there is a relationship between mesh stiffness and carrier gear. As it is shown, the momentum of inertia J_r (ring gear) has a derivative causality; this is due to a fixed ring stage consideration; it means that a $Sf = 0$ source is bounded (at the 1_5 junction) in order to impose a non-angular velocity at this stage of planetary gearbox. In the model, Z_i ($i = \mathrm{p, s, r}$) represents the teeth number of each gear. The sun output is bonded to TF element, which represents the two parallel stages output. This model allows a design of the gearbox, using the parameter estimation concept developed in [30].

The flow junction $1_{1\to3}$, 1_4, 1_5, 1_6 represents the angular velocity of planets, carrier, ring, and sun gear, respectively. They are all related to each other by TF elements.

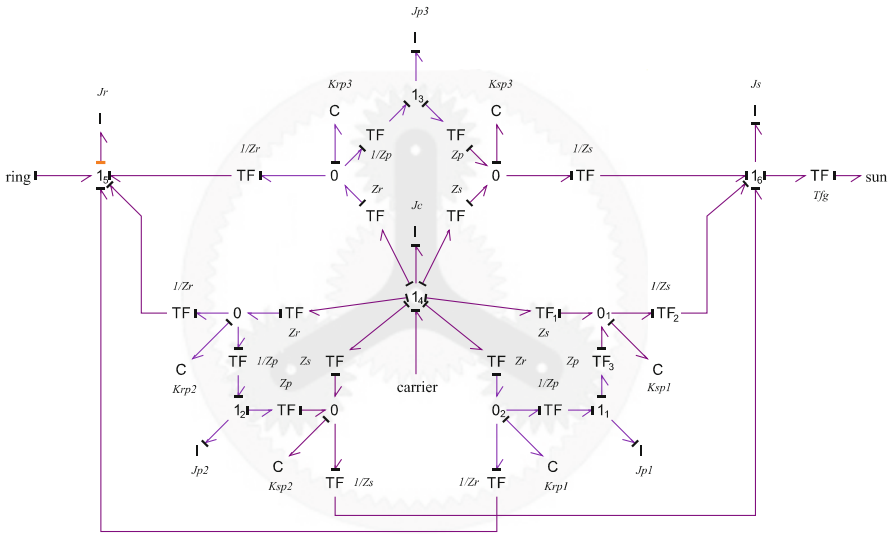

Fig. 15.12 Gearbox model

Considering the planet 1 (see Fig. 15.12), it is shown that there is a zero junction 0_1, between the transformer TF_1, TF_2, and TF_3, which represents (effort variable) that the planet moves in tangential direction. In this junction, the mesh stiffness between the planet and sun is joined. Transformers TF_1:Z_s, TF_2:$1/Z_s$, and TF_3:Z_p allow to obtain the rotating speed of the sun gear, the linear velocity of the planet revolution around the sun gear, and the planet autorotation. This structure is the same for the zero junction 0_2, but considering the relationship between the planet, the ring, and the carrier.

If a more precise model of a gearbox is required, the design can be done as it was made for the blade model. This means that the gears can be taken as a structure, considering their mass and the translational displacement. Also, bearing stiffness and torsional support stiffness can be added to the model.

The main dynamics representation can be directly achieved. Opposite to blade structure, gearbox of Fig. 15.12 does not have causal's loops, since nonresistive elements (bearings) are considered. Thus, only a path loop between the inertial gears and the mesh stiffness can be found. Parameters (see Appendix) for a 750 kW wind turbine gearbox are used and have been taken from [13].

15.3.2.2 Gearbox Simulation

One simulation is carried out in order to verify the gearbox model. Table 15.2 shows the numerical values used for the simulation. Torque and angular velocity for sun and carrier are shown in Fig. 15.13.

Table 15.2 Gearbox numerical values

Gearbox
$J_s = 3.2$ kg.m^2, $J_r = 144.2$ kg.m^2, $J_c = 59.1$ kg.m^2, $J_p = 3.2$ kg.m^2
$Z_p = 39$, $Z_r = 99$, $Z_s = 21$, $K_{sp} = 16.9$e9 N/m, $K_{rp} = 19.2$e9 N/m, $T_{fg} = 10.5$

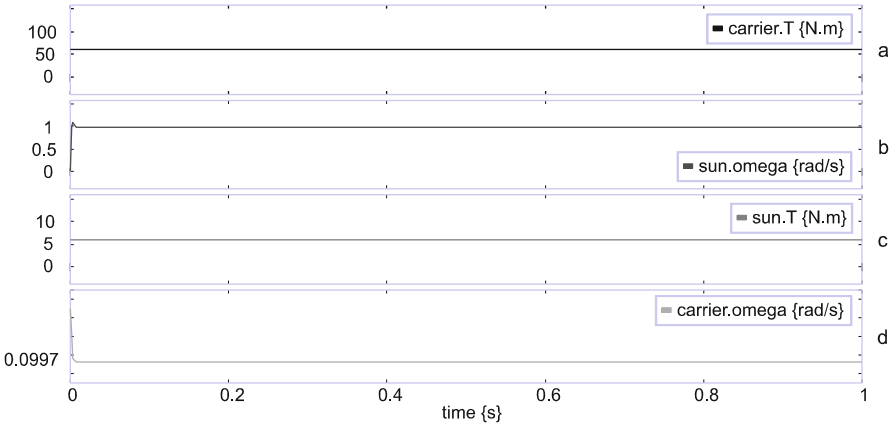

Fig. 15.13 Simulation gearbox (**a**) carrier torque, (**b**) sun torque, (**c**) sun angular velocity, and (**d**) carrier angular velocity

For the simulation, a constant carrier torque is applied (Fig. 15.13a). This torque is reduced at the sun output torque with a ratio of 60 (Fig. 15.13c). The same case is observed in the angular velocity curves (Fig. 15.13b, d). It is known that this type of system presents a fast vibration, due to the dynamics involved between the mesh stiffness and the momentum of inertias. In Fig. 15.13, the initial conditions (for the momentum of inertias) have been considered, in order to show the conversion ratio of the gearbox. This allows eliminating these vibrations when simulation starts. Figure 15.13 verifies that the complete gain of gearbox is 60. This is an acceptable value of the gearbox gain; since a value of 60 or 70 is expected for a wind turbine with these dimensions (750 kW).

15.3.3 Doubly Fed Induction Generator

Induction machines have been addressed in many publications. Models can be represented in two general frameworks: one using a Park reference frame [18, 38, 39] and the other one using the natural reference frame (three sinusoidal waveforms) [28].

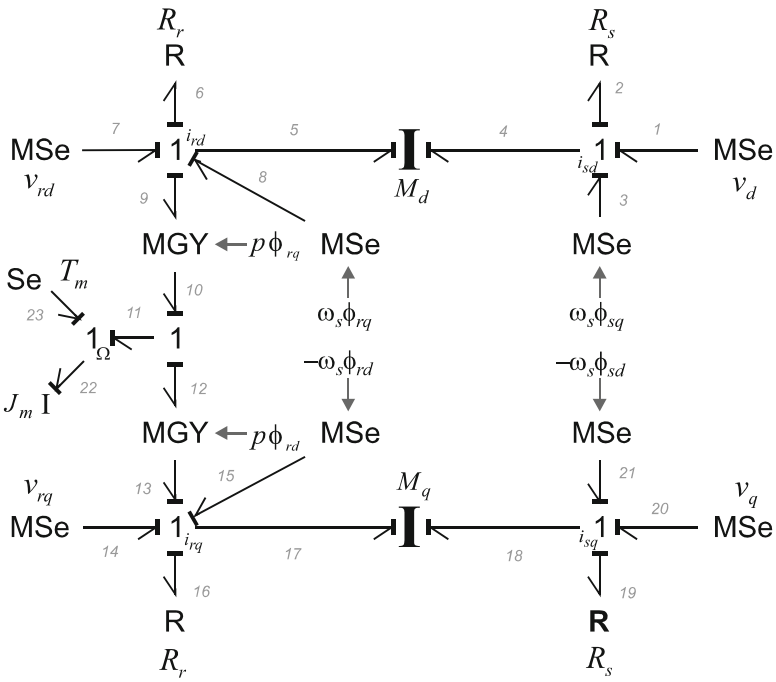

Fig. 15.14 DFIG 2-axis reference frame

15.3.3.1 Park Reference Frame Model

Figure 15.14 shows a bond graph model of the induction machine in the Park 2-axis *d-q* reference frame [38].

The induction machine model is based on the following assumptions:

- Magnetic hysteresis and magnetic saturation effects are neglected.
- The stator winding is sinusoidally distributed along the air-gap.
- The stator slots cause no appreciable variation of the rotor inductances with rotor position.

An arbitrary *dq-frame* rotating around the homopolar *0-axis* to the speed ω_s is chosen.

The equations that describe the bond graph model of Fig. 15.14 are given by Eq. (15.6).

$$\begin{aligned}
v_d &= R_s i_{sd} + \frac{d\varphi_{sd}}{dt} - \omega_s \varphi_{sq} \\
v_q &= R_s i_{sq} + \frac{d\varphi_{sq}}{dt} + \omega_s \varphi_{sd} \\
v_{rd} &= R_r i_{rd} + \frac{d\varphi_{rd}}{dt} - \omega_s \varphi_{rq} + p\Omega\varphi_{rq} \\
v_{rq} &= R_r i_{rq} + \frac{d\varphi_{rq}}{dt} + \omega_s \varphi_{rd} - p\Omega\varphi_{rd} \\
\tau_{11} &= p\left(\varphi_{rq} i_{rd} - \varphi_{rd} i_{rq}\right) \\
\tau_{11} &= J_m \frac{d\Omega}{dt} - T_m
\end{aligned} \tag{15.6}$$

The inductance matrices for I-field elements M_d and M_q allow coupling the stator and rotor fluxes by the matrix shown in Eq. (15.7).

$$\begin{pmatrix} \varphi_{sd/q} \\ \varphi_{rd/q} \end{pmatrix} = \begin{pmatrix} L_s & L_m \\ L_m & L_r \end{pmatrix} \begin{pmatrix} i_{sd/q} \\ i_{rd/q} \end{pmatrix} \tag{15.7}$$

where L_s, L_m, and L_r are the stator self-inductance, mutual inductance between the stator and rotor, and rotor self-inductance, respectively. I-field element J_m represents the shaft and rotor moment of inertia; R_s and R_r are stator and rotor resistances, p is the number of pole pairs, and ω corresponds to $2\pi f$, with f being the network frequency.

It is important to remark that the four modulated sources (dependent on ω_s) represent virtual sources (not physical sources), since their power sum is zero and are only a mathematical consequence of the model, as demonstrated in [18]. They are considered by the arbitrary framework assumption and can be removed if the stationary frame is chosen (setting *d-axis* with stator phase a) since $\omega_s = 0$. As the machine model is related to the rotor, the stator equations are not influenced by the rotor speed.

The model of the DFIG was developed by using the equivalent electric circuit of the induction machine shown in Fig. 15.15 [38].

15.3.3.2 Model Simplification

The methodology shown in [2] can be applied to the bond graph model of the induction machine, in order to reduce the order model from the energy metric point of view. However, since the application of the induction machine in the wind turbine (as a generator) does not involve a high rotor speed, it is assumed that the neglected mode cannot be excited.

In order to identify the dynamics that can be eliminated, the dynamics approximation made before with the blade structure is applied to the DFIG. Since the model has I-field multiports, the dynamics are obtained by using the methodology proposed in [20], which allows obtaining the causal loops and paths when a multiport is used.

The dynamic model can be simplified through an algebraic equivalent. This can be achieved if the dynamics are eliminated, the transient is cancelled and the order of the model is reduced. Thus, by setting $\dot{\varphi}_{sq}$ and $\dot{\varphi}_{sd}$ equal to zero, the model order is reduced from 5 to 3.

Regarding Fig. 15.14, the causality change is required in bonds 4 and 19. Figure 15.16 shows the stator *d/q-axis* simplified model of the induction machine.

Effort in bond 4 is zero, since the stator dynamics are eliminated. As the current i_{sd} is used to calculate the flux φ_{sd} (necessary for the MSe source along *q-axis*), the same structure is kept, and only the causality is changed. A similar process is made in bond 19.

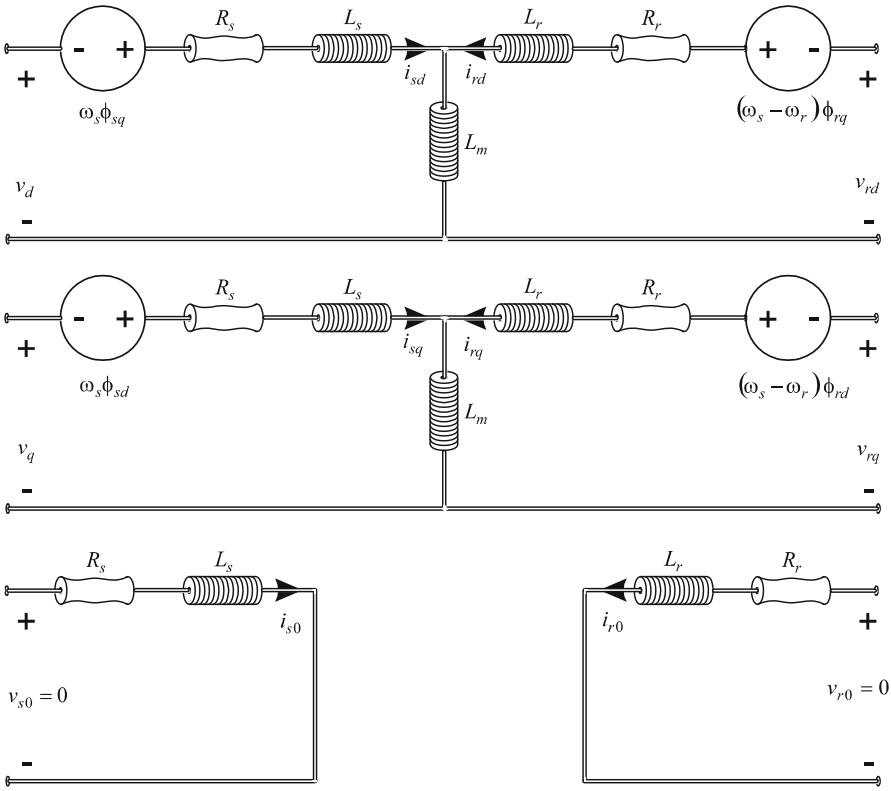

Fig. 15.15 Induction machine electrical circuit in dq_0 arbitrary frame

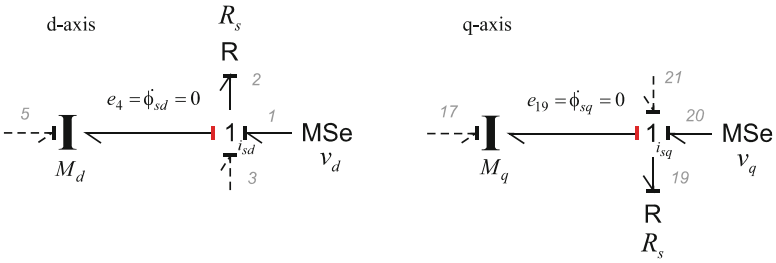

Fig. 15.16 Stator d, q-axis simplified

Table 15.3 Doubly fed induction machine parameters

Power	750 kW	Stator inductance	2.51 mH
Poles numbers	2	Rotor inductance	2.45 mH
Voltage	690 V	Mutual inductance	2.41 mH
Stator resistance	0.0022 Ω	Inertia	63.89 kg.m^2
Rotor resistance	0.0018 Ω	Frequency	60 Hz

Causality changes require a modification of (15.7). Matrix expressions in the I-field elements are changed to:

$$\begin{pmatrix} \varphi_{sd,q} \\ i_{rd,q} \end{pmatrix} = \begin{pmatrix} L_s - \frac{L_m^2}{L_r} & \frac{L_m}{L_r} \\ -\frac{L_m}{L_r} & \frac{1}{L_r} \end{pmatrix} \begin{pmatrix} i_{sd,q} \\ \varphi_{rd,q} \end{pmatrix} \tag{15.8}$$

Causality changes reduce from 5 to 3 the number of independent state variables in the model. The dynamic equation in the stator part is changed for a static one, and the effort is set equal to zero in these bonds.

15.3.3.3 DFIG Simulation

In order to compare the behavior of the simplified model (order 3) against the complete one (order 5), a simulation is carried out by considering the doubly fed induction machine as a motor (DFIM). Table 15.3 shows the numerical parameters for the machine.

The DFIM is started at instant $t = 0$ s, then at $t = 6.5$ s the nominal torque is applied ($T_{\text{nom}} = 3978.88$ Nm). After that, at $t = 8.0$ s a voltage reduction of 50 % during 200 ms is applied. Figure 15.17 shows the obtained results.

As observed from Fig. 15.17, the response obtained with both models is in close agreement. It is important to observe that oscillations are eliminated when the simplified model is used. For example, the speed in the complete model ("speed Comp," Fig. 15.17a) oscillates at the instant voltage falls; these are eliminated in the simplified model (speed Simp). A more pronounced difference between models is observed at the machine starting (Fig. 15.17b).

It is important to mention that the simulation of the DFIM is made considering the two sources input: one for the stator (v_{d}, v_{q}) and the other for the rotor (v_{rd}, v_{rq}).

If nominal values around the equilibrium point are assumed, pole location analysis can be performed. Table 15.4 shows the pole values for the two models. By using these values, it is verified again that the change of causality (Fig. 15.16) and dynamics elimination ($\dot{\varphi}_{sq} = \dot{\varphi}_{sd} = 0$) allow to obtain a model without oscillations.

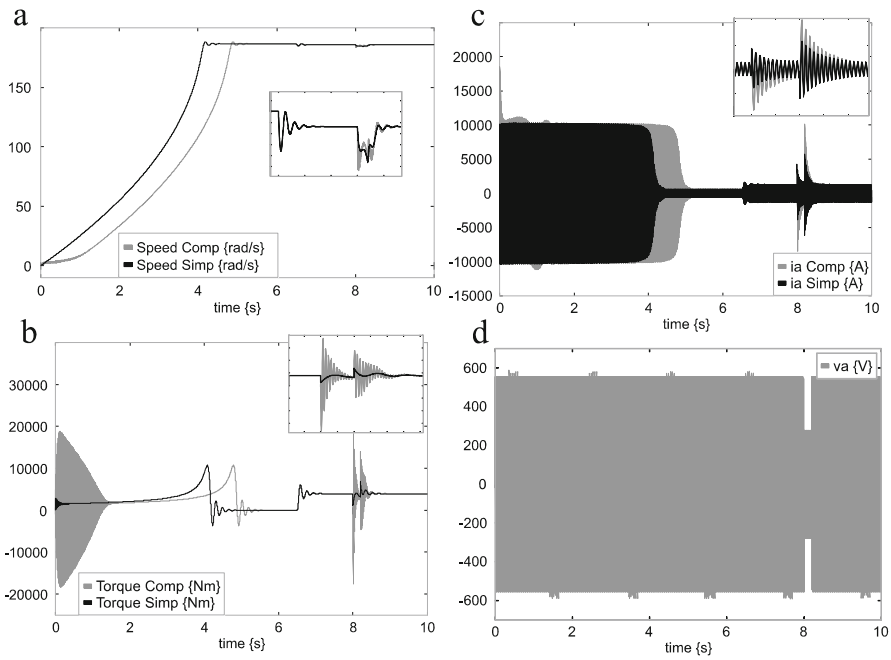

Fig. 15.17 Comparison responses of the complete (comp) and simplified (simp) DFIM, (**a**) speed, (**b**) torque, (**c**) current phase a, and (**d**) voltage input phase a

Table 15.4 Numerical pole values for complete and simplified model

Complete DFIM Model	Simplified DFIM Model
$P_1 = -6.8 + 35.9\text{i}$	$P_1 = -6.86 + 35.9\text{i}$
$P_2 = -6.8 - 35.9\text{i}$	$P_2 = -6.86 - 35.9\text{i}$
$P_3 = -12.4$	$P_3 = -12.39$
$P_4 = -15.69 + 376.5\text{i}$	
$P_5 = -15.69 - 376.5\text{i}$	

15.3.4 Power Electronic Converter

The three phase converter model has been addressed in many papers, such as [12, 23]. Each presented model has its own characteristic and is used for different applications.

15.3.4.1 Power Converter Model

As said before, two power electronics converters, the machine side converter (MSC) and network side converter (NSC), are used in order to have a DC-link between them allowing the power transfer.

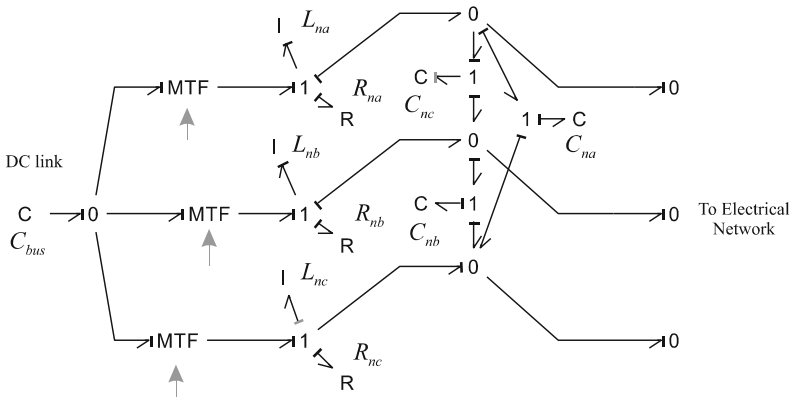

Fig. 15.18 Network side converter with a three phase LC filter

For the NSC, the model is taken from [42, 43]. This model corresponds to a three phase converter using an LC filter connection. The filter allows to give a voltage source behavior for the converter, and also to eliminate the harmonic distortion introduced by the converter. Figure 15.18 shows the NSC used.

The characteristics of the model are the DC-link is considered as a dynamical element (C_{bus}), and the LC filter is composed of three inductances with their associated resistances and three Delta connected capacitors.

The causality assignment gives to the power electronic converter associated with the LC filter a voltage source behavior.

In the next section it will be presented the control law necessary to transfer the active and reactive power to the network.

15.4 Control of the Doubly Fed Induction Generator

As previously shown, the induction machine is a coupled 5th or 3th order system (depending on the considered model) with four inputs. Actually, the simplification made in the previous section allows to intuitively knowing that stator dynamics are not directly involved in the control law. For that reason, the control inputs which are present in the doubly fed induction machine are those of rotor. The last assumption is commonly made when a generator control law is deduced, but here, the bond graph model supports this assumption.

15.4.1 Torque Control Formulation (Machine Side Converter)

When a wind turbine generator is used, the objective is to control the output torque. Also, the torque can be controlled indirectly by the speed. This selection will be dependent on the particular application.

It is important to remark that the proposed control does not consider the Sommerfeld effect [40, 41], since unbalance rotor conditions are not considered.

In order to control the output torque, it is necessary to control the *d-axis* rotor flux supplied by the DFIG. To this aim, a specific algorithm is designed, based on bicausal bond graph [11].

For the formulation of the inverse bond graph, it is necessary to change the effort detectors De (assumed ideal), which will be placed in bond 5 of Fig. 15.14 in the original bond graph, by a source named SS, (which impose zero flow but non-zero effort to the inverse model), then propagate bicausality (in only one line of power transfer) from this source (SS: $\dot{\varphi}_{\mathrm{rd}}$) to the input source of the original bond graph which becomes a detector (i.e., SS: v_{rd}) in the inverse bond graph [31].

The structure of the control in open loop is designed with the inverse bond graph. The decoupling actions are defined (inverse matrix and disturbance compensation). The open loop structure is then extended to a closed loop control by fixing the dynamics of errors.

Figure 15.19 shows the preferred derivative causality assigned in the inverse bond graph, which allows to deduce the open loop control laws. The rotor flux and torque sensors are simultaneously inverted via bicausal bonds; two disjoint bicausal paths are drawn to the two desired inverse model outputs, corresponding to the two control signals (MSe:v_{rd}, MSe:v_{rq}), which demonstrates that the model is invertible [31]. It is important to notice that the J_m inertia is not considered in the inverse bond graph of Fig. 15.19. This is because non-unbalanced rotor operation has been considered and because this inertia will represent the whole wind turbine inertia.

For the rotor flux control law, no change is presented in the I-field element M_{d}. Otherwise, the causality change in bond 4 is due to the simplified model consideration (this bond has not a dynamic behavior). Equation (15.9) is derived from the inverse bond graph of Fig. 15.19, and this relationship corresponds to the 1-junction placed between bonds 5, 6, 7, 8, and 9.

$$-e_6 + e_7 + e_8 - e_9 = e_5 \tag{15.9}$$

It is assumed that the numerical value of the elements (resistances and inductances) is the same for 2 axes. These values have been taken as estimated values, e.g., $\widehat{R}_r$ of the actual system parameters, in order to consider a slight error. By replacing these values in (15.4) it gives

$$v_{\mathrm{rd}} = \frac{\mathrm{d}}{\mathrm{d}t}\varphi_{\mathrm{rd}} + \widehat{R}_r i_{\mathrm{rd}} + p\varphi_{\mathrm{rq}}\Omega - \omega\varphi_{\mathrm{rq}} \tag{15.10}$$

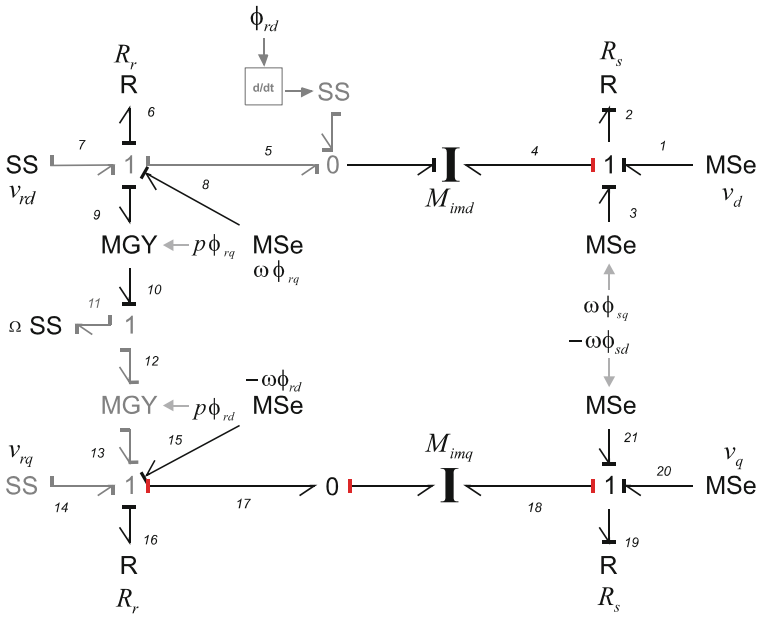

Fig. 15.19 Inverse DFIG for calculation of the controls laws

To establish the closed loop control law, the dynamics of the error ($\varepsilon = \varphi_{\text{rqref}} - \varphi_{\text{rq}}$) are set in (15.10), as $\dot{\varepsilon} + k_1\varepsilon = 0$, where k_1 represents the controller to be used. Expression (15.10) becomes (15.11) as:

$$v_{\text{rd}} = \frac{\text{d}}{\text{d}t}\left(\varphi_{\text{rdref}} - \varepsilon\right) + \widehat{R}_r i_{\text{rd}} + p\varphi_{\text{rq}}\Omega - \omega\varphi_{\text{rq}} \tag{15.11}$$

Finally,

$$v_{\text{rd}} = \frac{\text{d}}{\text{d}t}\varphi_{\text{rdref}} + k_1\left(\varphi_{\text{rdref}} - \varphi_{\text{rd}}\right) + \widehat{R}_r i_{\text{rd}} + p\varphi_{\text{rq}}\Omega - \omega\varphi_{\text{rq}} \tag{15.12}$$

For the last expression, the rotor flux φ_{rq} is assumed to be zero. This is justified since φ_{rq}, compared to φ_{rd} has not an important impact on the voltage v_{rd}. Actually, this value is very small compared to the *d-axis* flux.

Taking the last consideration, (15.12) is represented in the Laplace domain as,

$$(v_{rd})_{(s)} = s(\varphi_{\text{rdref}})_{(s)} + k_1(\varphi_{\text{rdref}} - \varphi_{\text{rd}})_{(s)} + \widehat{R}_r(i_{\text{rd}})_{(s)} \tag{15.13}$$

In the same manner as for the determination of the rotor flux control, the torque control law is calculated.

Equation (15.14) is derived from the bond graph of Fig. 15.19 as,

$$e_{14} - e_{18} + e_{15} + e_{13} - e_{17} = 0 \tag{15.14}$$

For (15.14), the effort e_{17} needs to be calculated from (15.8), by assuming that $\varphi_{\mathrm{rq}} = \int e_{17}$. Making the appropriate substitutions in (15.14), it yields,

$$v_{\mathrm{rq}} = \widehat{L}_r \frac{\mathrm{d}}{\mathrm{d}t} i_{\mathrm{rq}} + \widehat{R}_r i_{\mathrm{rq}} - p\varphi_{\mathrm{rd}}\Omega + \omega\varphi_{\mathrm{rd}} \tag{15.15}$$

In (15.15), the current i_{sq} of (15.8) has been assumed zero, since the balanced condition of the Park transformation has been considered. However, the mutual inductance is not present in (15.15).

The voltage v_{rq} and torque relation are not explicitly shown in (15.15). Thus, in order to relate (15.15) with the torque, another expression is needed.

Two different procedures are visualized, i.e., the first is to replace the speed Ω for his equivalent relation with the torque, and the second one is to establish an internal control loop for the i_{rq} current, and cascade the torque relationship in the previously internal control loop.

The second solution is chosen, since it provides a control law structure similar to the traditional vector control [49] applied to this machine.

By using the estimated values and establishing the closed control loop (for i_{rq} variable) as previously described, (15.15) becomes,

$$v_{\mathrm{rq}} = \widehat{R}_r i_{\mathrm{rq}} - p\varphi_{\mathrm{rd}}\Omega + \omega\varphi_{\mathrm{rd}} + \widehat{L}_r \frac{\mathrm{d}}{\mathrm{d}t} i_{\mathrm{rqref}} + \widehat{L}_r k_2 \left(i_{\mathrm{rqref}} - i_{\mathrm{rq}}\right) \tag{15.16}$$

where k_2 represents the controller used for this loop. The other necessary expression is taken from the original model (Fig. 15.14); specifically, in bond 11 the torque is given by,

$$T_{e11} = p\left(\varphi_{\mathrm{rq}} i_{\mathrm{rd}} - \varphi_{\mathrm{rd}} i_{\mathrm{rq}}\right) \tag{15.17}$$

As $\varphi_{\mathrm{rq}} = 0$, expression (15.17) becomes $T_{e11} = -p\varphi_{\mathrm{rd}} i_{\mathrm{rq}}$, and can be expressed as $T_{\mathrm{ref}} = -p\varphi_{\mathrm{rd}} i_{\mathrm{rqref}}$. This expression is replaced in (15.16), to obtain the control law (15.18).

$$\left(v_{\mathrm{rq}}\right)_{(s)} = \widehat{R}_r \left(i_{\mathrm{rq}}\right)_{(s)} - p\varphi_{\mathrm{rd}}\Omega + \omega\varphi_{\mathrm{rd}} + \widehat{L}_r s \left(\frac{T_{\mathrm{ref}}}{-p\varphi_{\mathrm{rd}}}\right)_{(s)} + \widehat{L}_r k_2 \left(\frac{T_{\mathrm{ref}}}{-p\varphi_{\mathrm{rd}}} - i_{\mathrm{rq}}\right)_{(s)} \tag{15.18}$$

The controller block diagram (Eqs. (15.13) and (15.17)) is shown in Fig. 15.20. It is important to notice that the structure of the control law contains a feed-forward with a derivative action on the reference signals. The signals are constants, so that they can be removed, and by taking into consideration that the wind does not have a sudden change, they are kept in this proposed control law. In addition, the control law needs an estimation of φ_{rd}, then the expression $(L_{\mathrm{s}}{*}i_{\mathrm{rd}} + L_{\mathrm{m}}{*}i_{\mathrm{sd}})$ [49] is used.

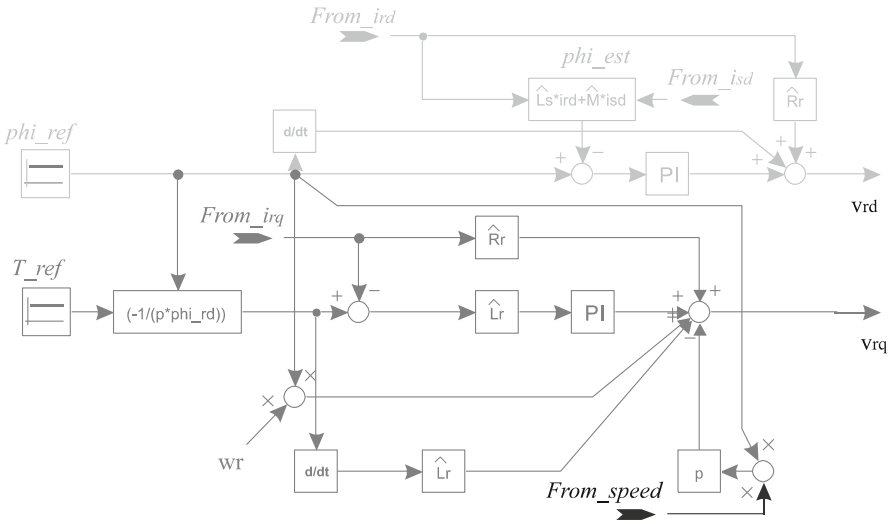

Fig. 15.20 Torque control law schema

15.4.2 Torque Control Simulation

In order to verify control law, a simulation is carried out by considering that the DFIG has a primary governor to emulate the torque provided by the turbine mechanical part. Also, as it is considered that the converter has not an important impact in the machine behavior, the machine side converter is not used. This allows to connect the v_{rd} and v_{rq} voltages directly via the MSe sources. Figure 15.21 shows the simulation scheme.

The stator machine power is regulated by the rotor. In order to simulate the DFIG, a three phase load is connected at machine terminals. Park's transformation is used in order to transform from the *dq* reference frame to the *abc* framework.

The complete DFIG model is used in the simulation. The results presented here have been verified against the simplified DFIG model, obtaining the same results; the only difference being that the oscillations due to the fast dynamics are present in the complete model.

A speed governor is used to maintain the nominal speed in the generator. As the objective is to test the behavior of the control law; this stage has been represented by using an ideal Governor (PI controller).

Results are shown in Fig. 15.22. Numerical values of Tables 15.3 and 15.5 are used for the simulation. The DFIG is started at instant $t = 0$ s applying the nominal torque as reference in the control ($T_{ref} = 3978.88$ Nm), then at $t = 5$ s the nominal torque is reduce to $T_{ref} = 2500$. This is made in order to observe that the torque in the machine is also reduced.

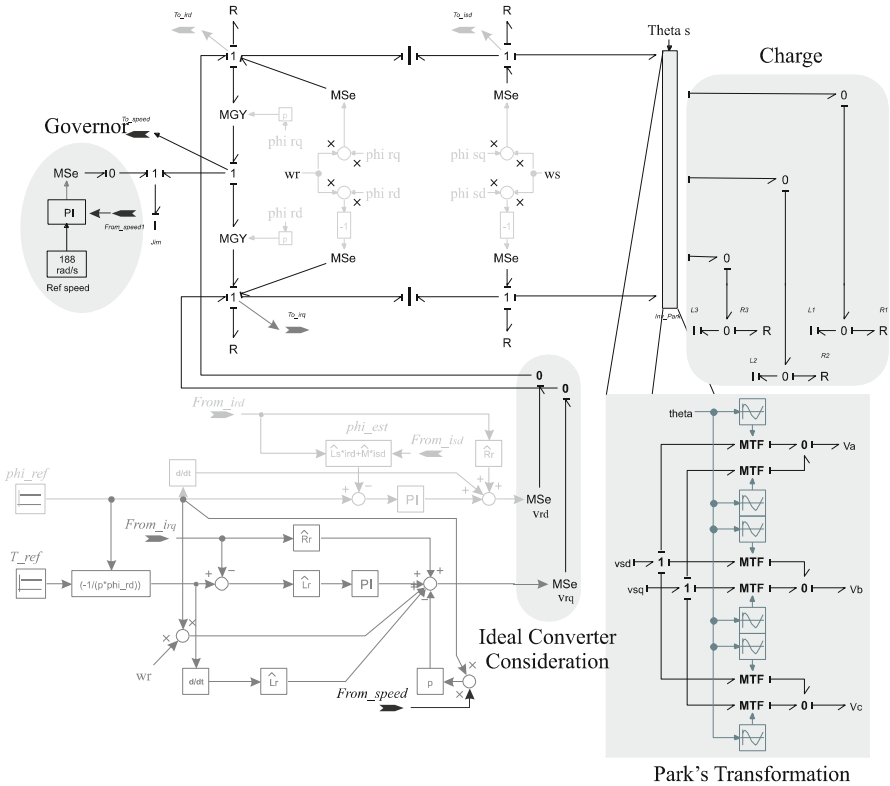

Fig. 15.21 Simulation schema for the DFIG—constant speed

The charge was selected to have a power factor of 0.8, and how is shown in Fig. 15.22d the total active power is supplied to the charge when the nominal torque is set in the reference control, and is reduced when the torque decreases.

15.4.3 Robustness Test

In order to verify the robustness of the proposed control law, the simulation schema presented before is used (Fig. 15.21).

The pole-plot can be taken directly from the simulator. Then, in order to verify the robustness of the control, different values of power factor in the load (0.5–1) are used. The nominal values of torque and the magnetic flux (T_{ref} and phi_{ref} in Fig. 15.21) have been considered by taking into account the parameters of Table 15.3 and Table 15.5. Figure 15.23 shows the 3D pole-plot evolution.

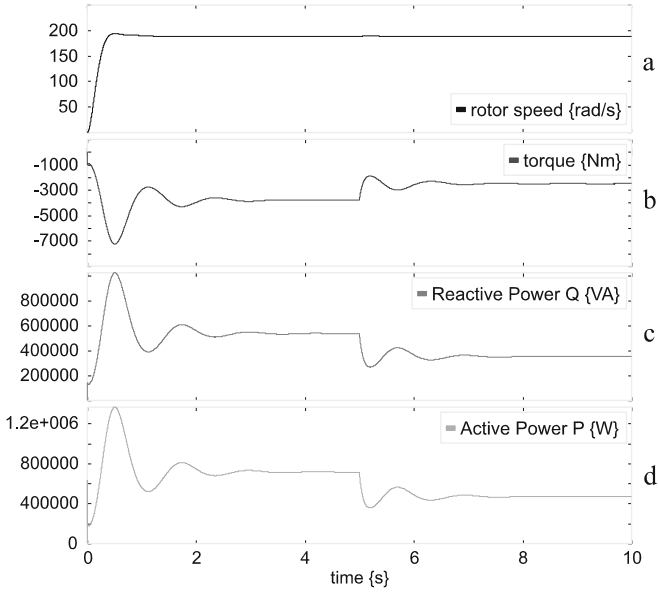

Fig. 15.22 DFIG responses, (**a**) Machine speed, (**b**) torque, (**c**) reactive power in the charge, and (**d**) active power in the charge

Table 15.5 Control and charge numerical values

Control	Charge	
PI v_{rd}	PI v_{rq}	
$K_p = 1000$	$K_p = 150$	$R_{1,2,3} = 0.5078\,\Omega$
$K_i = 1$ m	$K_i = 10$ m	$L_{1,2,3} = 1.01$ mH

Poles which have a significant movement correspond to the load poles. Unlike the generator and control poles, these do not have a significant movement when the power factor is varied. This shows the robustness of the proposed control in this system. It is important to mention that in order to take into account the uncertainties due to parameter estimation the simulation is carried out by assuming a slight error in the parameters, i.e., 10 % between the model and the controller parameters.

15.4.4 Network Side Converter

As said before, the three phase NSC uses an LC filter in order to impose a voltage behavior in the converter.

The structure of the converter was presented in Fig. 15.18. Then in this section, the active and reactive power control is presented.

The control law of this converter is also derived from the inverse bond graph (using the bicausality concept); the robustness and accurate performance of the

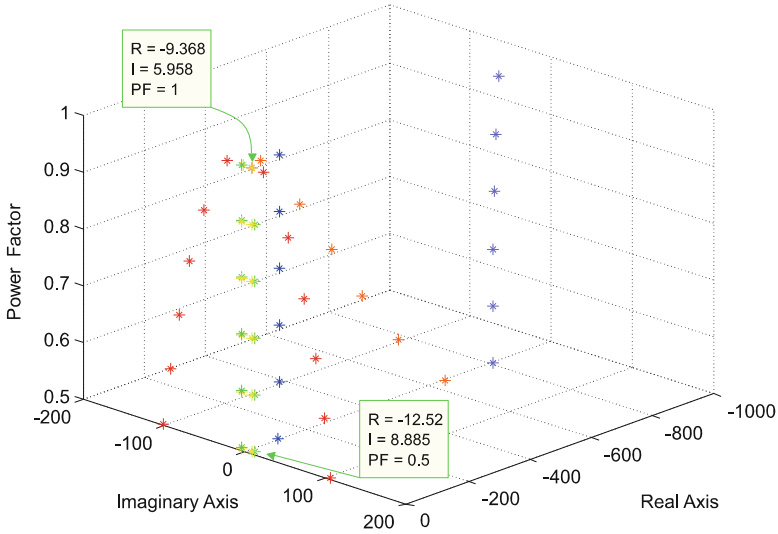

Fig. 15.23 3D pole-plot evolution

proposed control has been demonstrated for voltage regulation [42]. Here, the highlights of this control are recalled. They are as follows:

- The controller parameters are obtained considering the two loops in cascade, one for the current in the L_{ni} and another one for the voltage in C_{ni}-elements.
- Only two phase to phase voltages are considered in the control, the third one fixing the voltage reference.
- The current i_{nc} is linearly dependent on the two others (i_{na} and i_{nb}).
- The average behavior of the converter is considered.

The control is composed by three principal stages:

1. DC bus regulation. It is based on a traditional PI (proportional + integral) controller. It provides the active power reference.
2. Active and reactive power regulation. Inspired from the power flow concept between two sources, connected through a line impedance.
3. Voltage and current regulation. A resonant and proportional controller for voltage and current control, respectively.

Figure 15.24 resumes the control stages for the NSC.

From Fig. 15.24, the source V_{dcref} sets the DC-link regulation reference, the i_{bus} and v_{bus} are necessaries in order to have the total power available in the DC-link. Since this power provides the active power reference. In the right side of Fig. 15.24 it can see three I-elements connected in series with their respective R-elements. These elements represent the line impedance, and are necessaries in order to apply the power flow concept.

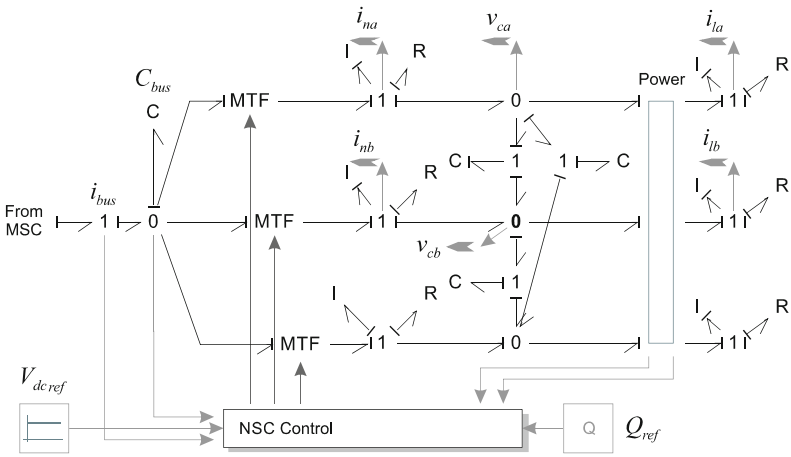

Fig. 15.24 Control schema simulation for the NSC

Finally in Fig. 15.24 it can be identified by a block connected between the delta connection capacitors (C-elements) and the line impedance. Inside this block is implemented Eqs. (15.19) and (15.20) which allows to get the active and reactive power measures.

$$P = v_{\mathrm{na}} i_{\mathrm{na}} + v_{\mathrm{nb}} i_{\mathrm{nb}} + v_{\mathrm{nc}} i_{\mathrm{nc}} \tag{15.19}$$

$$Q = \left(\left(v_{\mathrm{na}} - v_{\mathrm{nb}} \right) i_{\mathrm{nc}} + \left(v_{\mathrm{nb}} - v_{\mathrm{nc}} \right) i_{\mathrm{na}} + \left(v_{\mathrm{nc}} - v_{\mathrm{na}} \right) i_{\mathrm{nb}} \right) / \sqrt{3} \tag{15.20}$$

15.4.4.1 Active and Reactive Power Control

In case of connection with an infinite voltage source, the power control loop is inspired from the power flow concept between two sources (v_{con} and v_{res}) connected by an impedance line $Z = R + jX$ [14]. Assuming that the transmission line has small resistance compared to the reactance ($R = 0$), the active power is given by,

$$\begin{aligned} P &= \tfrac{V_{\mathrm{con}} V_{\mathrm{res}}}{X} \delta_c \\ Q &= \tfrac{V_{\mathrm{con}}}{X} \left(V_{\mathrm{con}} - V_{\mathrm{res}} \right) \end{aligned} \tag{15.21}$$

where: V_{con} and V_{res} are, respectively, the RMS values for v_{con} and v_{res}, and δ_{c} is the phase of V_{con} versus V_{res}. Expression (15.21) shows that a small difference on the angle has a direct impact on the active power flow. The magnitudes difference has a direct impact on the reactive power. The active power control is defining the value for δ_c angle and the $\Delta V = V_{\mathrm{con}} - V_{\mathrm{res}}$ define the reactive power, as shown in the schematic diagram of Fig. 15.25.

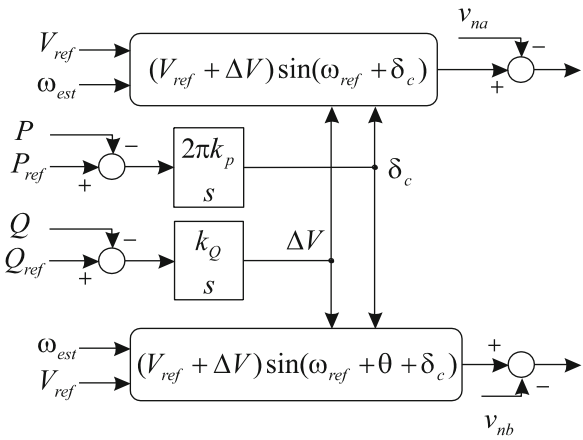

Fig. 15.25 Active and reactive power loop block diagram

In Fig. 15.25, k_P and k_Q are the gains in the controller, which have to be calculated taking into account the desired time response, ω_{est} is the grid pulsation, and V_{ref} is the network reference voltage.

15.5 Complete System

In this section the previously models are set up in order to simulate the complete system.

15.5.1 Simulation of a Variable-Speed Wind Turbine

The blades, gearbox, DFIG, and the power converters are associated in order to formulate the complete model of a variable-speed wind turbine as is shown in Fig. 15.26.

In Fig. 15.26, the block "Wind Turbine Model" corresponds to the blades and hub model of the turbine (Fig. 15.7). The gearbox model presented before (Fig. 15.12) is represented by the "GearBox" block. Also, Fig. 15.26 shows the whole control law involved in the variable-speed wind turbine. The block called "Wind control" corresponds to the wind turbine angular speed control. This control provides the reference torque, which is introduced in the torque control (Fig. 15.20) for the DFIG (Fig. 15.14). The active power is sensed in order to calculate the maximum power available in the mechanical part of the turbine. Then, this power is regulated via the pitch angle, given by the block "Pitch control." The block "NSC Converter (+Control)," groups the continuous voltage (DC-link), power, voltage, and current controls for the converter (Fig. 15.24).

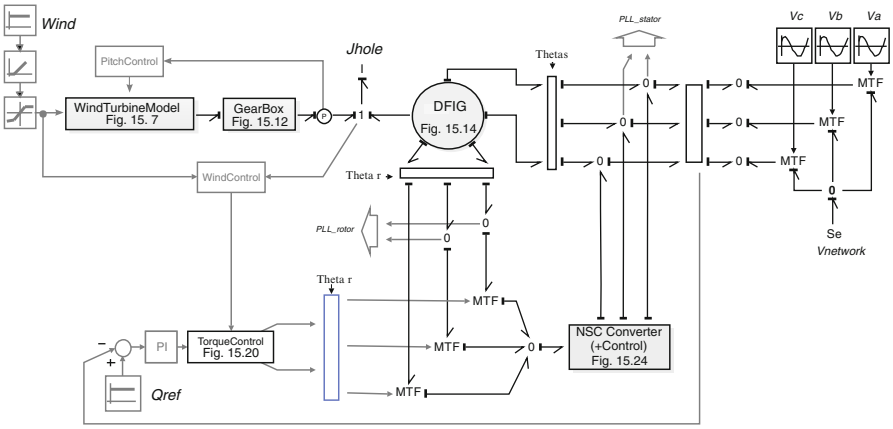

Fig. 15.26 Variable wind speed simulation model

It is important to mention that the control laws used for the angular speed and pitch angle of the blades have been taken from [34], and the NSC control from [42].

Additional elements such as power sensors, Park's transformation, and the phase lock-loop (PLL) are required to simulate the system. The turbine, the generator, and the power converter require sensors. For the turbine a power and angular speed sensors are used, while for the generator the rotor and stator currents sensors are needed to estimate the magnetic fluxes. These current sensors are also used in the power converter control.

In order to show the behavior of the complete model, two different simulations are conducted. First, a constant wind profile is considered, and then real wind profile data are used. As made before, these simulations have been performed using the 20Sim software.

15.5.2 Constant Wind Consideration

In this section the wind profile is considered constant with a ramp change in their speed.

The scenario for simulation is as follows: a constant wind of 5 m/s is applied at the simulation start; then, at $t = 10$ s, a wind ramp is applied. This wind ramp increases from 5 m/s, at $t = 10$ s to 15 m/s, at $t = 27.5$ s; this value is maintained until the simulation concludes. Figure 15.27a–c shows the simulation responses for the wind speed, DFIG speed, the tip speed, the power coefficient, the pitch angle, and the torque in the DFIG, respectively.

The speed in the DFIG increases in the same ratio as the wind input, i.e., up to the maximum value (226 rad/s) when the wind speed exceeds 12 m/s (see Fig. 15.27b). This is due to the fact that this value has been assumed to be the maximum set

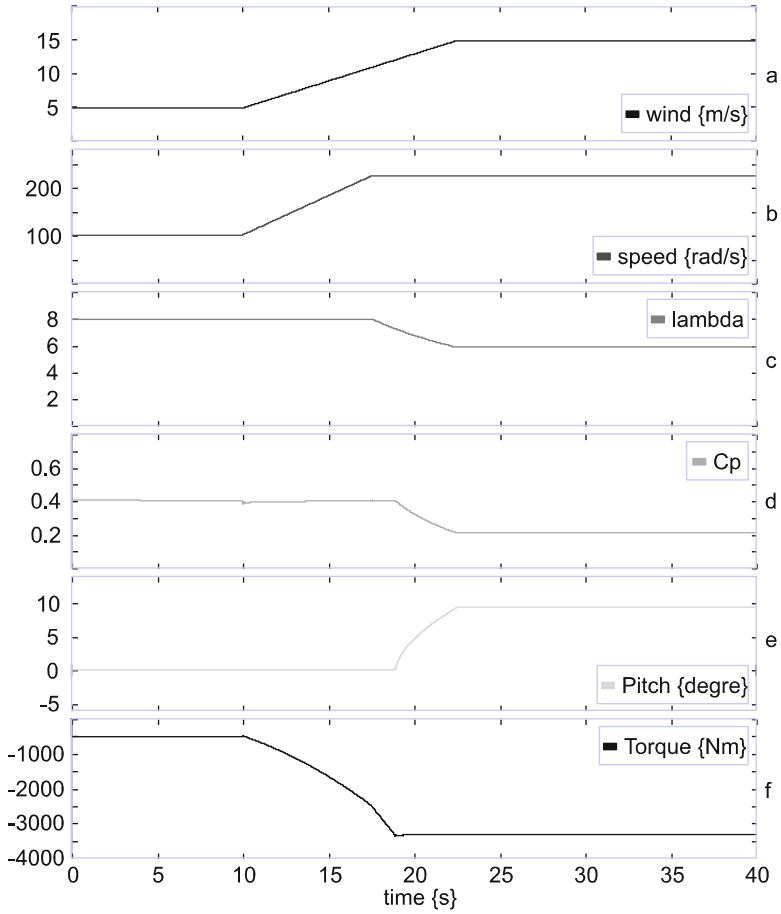

Fig. 15.27 Responses for a constant wind profile (**a**) wind, (**b**) DFIG speed, (**c**) λ, (**d**) power coefficient, (**e**) pitch angle, and (**f**) DFIG torque

point. The curve called "lambda" corresponds to the tip speed ratio, which presents its nominal value before the ramp profile starts (Fig. 15.27c). When machine speed increases to its maximum value, the tip speed decreases from 8 to 5.8. A similar case is shown for the power coefficient Cp (Fig. 15.27d). Figure 15.27e also shows the pitch angle applied to the blades, which starts at the instant when the wind speed exceeds 12 m/s. Finally, in Fig. 15.27f the actual torque in the generator is presented. There is a negative torque because the mechanical power is transferred to the power network, and their maximum value is −3315 Nm.

Active power needs to be provided by the wind turbine, and then distributed to the power network. Nevertheless, as a DFIM is used, the reactive power is present. Figure 15.28 shows the mechanical and electrical power in the wind turbine model. The power of the main shaft and the high speed shaft exactly match (750 kW); the

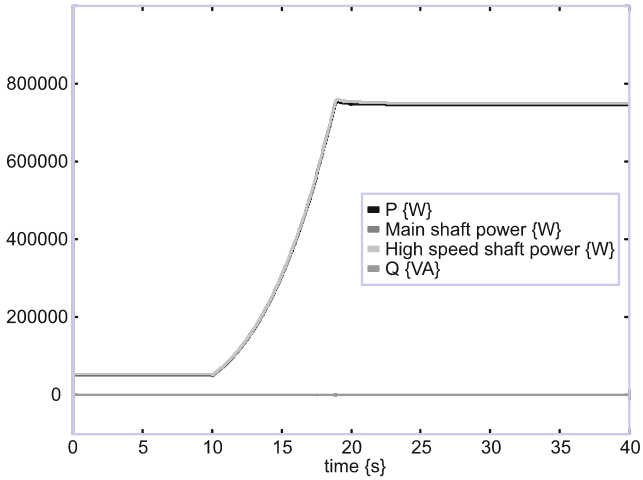

Fig. 15.28 Power curves for a constant wind profile

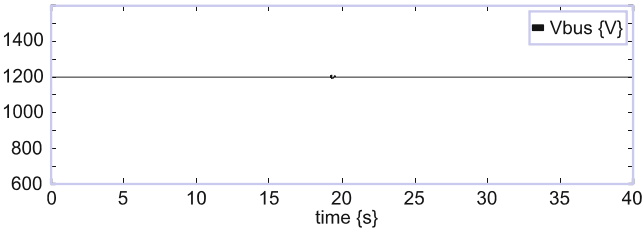

Fig. 15.29 Voltage in the DC-link for a constant wind profile

generator active power is closely to these ones (745 kW). This difference is due to the fact that estimated values for the generator have been calculated. Zero reactive power (Q) has been set as reference because not reactive power is absorbed by the network.

The regulation of the continuous bus is also an important parameter to take into consideration. Figure 15.29 shows the DC-link capacitor voltage, which follows the voltage reference (1200 V). It is important to mention that an initial condition is used in order to allow the simulation to be performed.

Figure 15.30 shows the three phase stator currents. A 460 V DFIG is used, with currents having larger values in order to meet active power demand.

The last simulation results allow the verification of theoretical concepts related to the wind turbine dynamic operation.

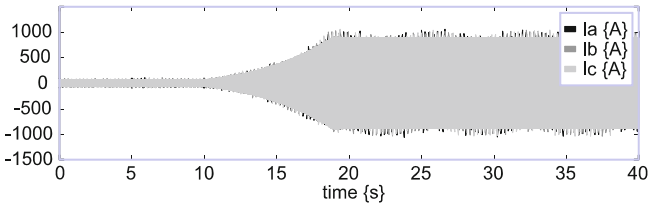

Fig. 15.30 Stator currents of DFIG—constant wind profile

15.5.3 Variable Wind Consideration

Practical wind behavior has a varying profile instead of being constant. The performance of the proposed control law can be confirmed if a real wind profile is used. Data are introduced in the simulator with a "data from file" block, which takes the numerical values from a table each time step. Figure 15.31 shows the simulation response for the selected wind turbine variables.

The wind changes (from 9 to 13 m/s) are reflected in the DFIG speed with the same ratio. When the wind crosses the limit of 12 m/s for small periods of time, i.e., from 10 to 60 s, the DFIG reaches its maximum value (226 rad/s). Also, this behavior is presented in the lambda (Fig. 15.31c), the Cp (Fig. 15.31d), and the pitch angle (Fig. 15.31e) responses.

In order to verify the generation of active power, Fig. 15.31e shows the actual torque. The torque arises to its maximum value when the wind speed increase (up to 12 m/s) or same, when the pitch angle increases.

Figure 15.32 shows the power curves for a real wind profile. Unlike the results presented with constant wind profile, in this simulation changes are observed in the power generated. As same as in the constant wind profile consideration, the main shaft and high speed shaft powers exactly match. Zero reactive power (Q) has also been set as reference.

The DC-link voltage is not presented, because is same as for the constant wind consideration (Fig. 15.29). Figure 15.33 shows the three phase currents supplied by the wind turbine to the network. Unlike the current results presented in the previous section, the changes in the magnitude are notorious.

The simulation results can verify that the proposed model and controls present a good performance, either for constant or variable wind speed. Nevertheless, some improvements can be suggested, as for example, the angular speed and pitch control needs to be improved. This is because they have been taken directly from [34], but need to be developed taking into account the model presented here.

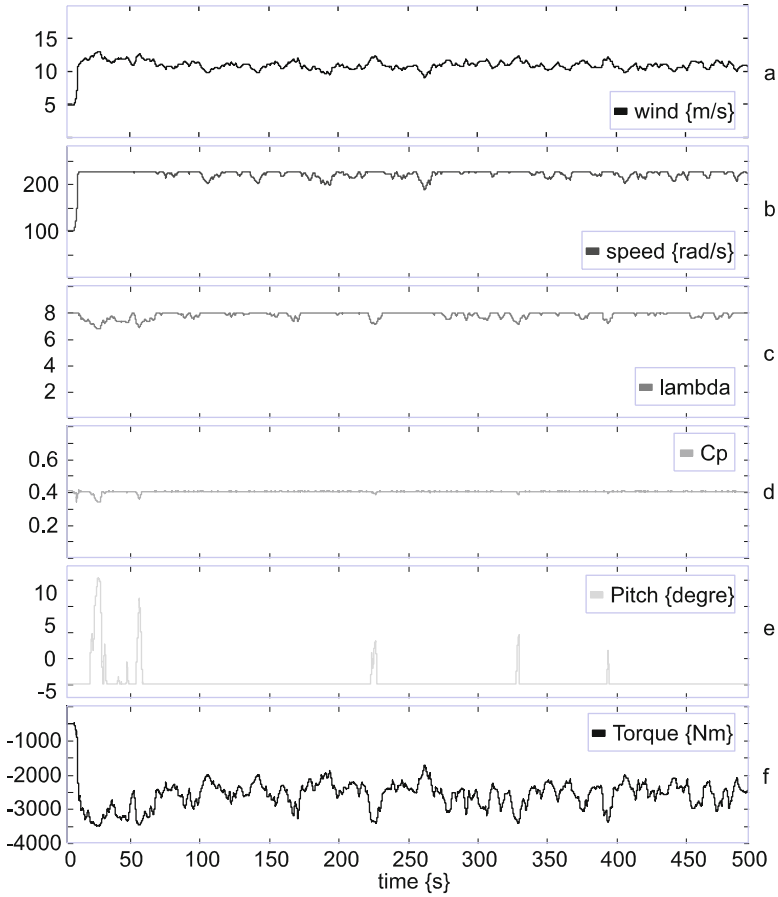

Fig. 15.31 Responses for a real wind profile (**a**) wind, (**b**) DFIG speed, (**c**) λ, (**d**) power coefficient, (**e**) pitch angle, and (**f**) DFIG torque

15.6 Conclusions

The complete model of a variable-speed wind turbine has been presented.

In order to apply the aerodynamic force, blade structure is considered to be a flexible body. BEM theory has been used for the wind aerodynamic force conversion. Values of torque and the coefficient of power in simulations have shown the validity of this model.

A gearbox model has been presented, where mesh stiffness between planet-sun and ring-planet are considered, and parallel stages are joined in only one stage. Power flows transferred by each stage has been presented in the simulation results.

For the DFIG, the causal loop concept applied to the model allowed to identify the dynamics (slow and fast) of the model approximation. Then, by choosing the

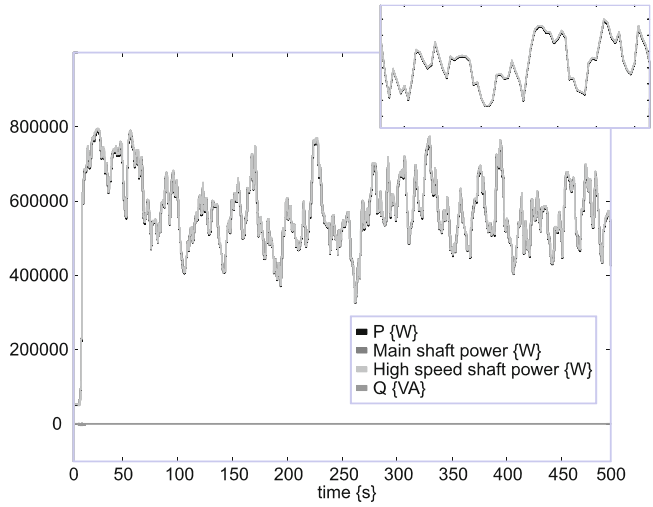

Fig. 15.32 Power curves for a real wind profile

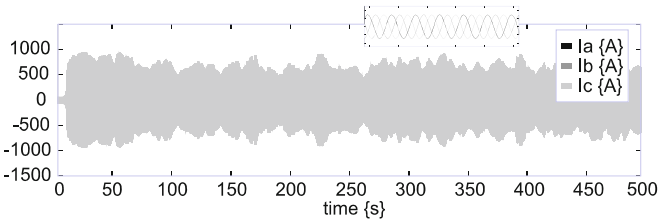

Fig. 15.33 Stator currents of DFIG—real wind profile

elimination of the fast dynamics, in order to reduce the order of the model, the simplified DFIG model has been used. By applying the bicausality concept, the simplified model has been used in order to formulate the inverse bond graph. The control laws were intuitively obtained by considering the simplified model.

As the proposed control law strongly depends on the estimated DFIM parameters, a traditional pole-place analysis has been conducted in order to verify the robustness of the control. The small error considered in the parameters did not vary the pole-place diagram.

The wind turbine behavior was simulated in order to verify the dynamic performance of the whole system. It has been demonstrated, via these simulations, that the proposed model yields good results; for real and for a constant wind consideration. Nevertheless, this model needs to be subjected to different tests, i.e., turbulent wind, gearbox faults, etc., in order to know the model performance.

It is suggested to test the proposed control law in a real-time simulator, in order to make a validation still closer to reality, before being tested in a real wind turbine.

Only a few publications involving all the stages of a wind turbine can be found in the open literature. In this context, the model presented here is an important starting point for the analysis of this complex system.

Appendix

Table 15.6 Wind turbine data

Hub and main shaft	
$J_{hub} = 5000$ kg.m^2, $D_{hub} = 1000$ N/m, $K_{ms} = 3.67e7$ N/m, $D_{ms} = 200$ N/m	
High speed shaft	
$K_{hs} = 10e7$ N/m, $D_{hs} = 1e-3$ N/m	
Blade structure data	
Section 1	Section 2
$E = 1.7e10$	$E = 1.7e10$
$l = 11.7$ m	$l = 11.7$ m
$M = 120.8$ kg	$M_2 = 48.7$ kg
$J = 3.3$ kg.m^2	$J_2 = 2.33$ kg.m^2
$\mu = 0.01$	$\mu = 0.01$
$J_{whole} = 1000$ kg.m^2	
Blade aerodynamic conversion	
$c_1 = 1.9$	$c_2 = 1$
$\beta_{t1} = 11$ deg	$\beta_{t2} = 1.7$ deg
$\rho_{air} = 1.225$	$\rho_{air} = 1.225$
$r_1 = 5.85$ m	$r_2 = 17.5$
$l_1 = 11.7$ m	$l_2 = 11.7$ m

References

1. Agarwal, S., Chalal, L., Dauphin-Tanguy, G., & Guillaud, X. (2012). Bond graph model of wind turbine blade. *IFAC Proceedings Volumes, 45*(2), 409–414.
2. Borutzy, W. (2011). *Bond graph modelling of engineering systems: Theory, applications and software support*, Chapter 2. New York: Springer Science Business Media, LLC.
3. Brown, F. (2001). *Engineering system dynamics*. New York: Marcel Dekker. ISBN 0-8247-0616-1.
4. Buhl, M. L. Jr. (2004). *A new empirical relationship between thrust coefficient and induction factor for the turbulent windmill state*. NREL/TP-500-36834. Golden, CO: National Renewable Energy Laboratory.
5. Burton, T., Sharpe, D., Jenkins, N., & Bossanyi, E. (2001). *Wind energy handbook* (p. 11). New York: Wiley.
6. Coudert, N., Dauphin-Tanguy, G., & Rault, A. (1993). Mechatronic design of an automatic gear box using bond graphs. In *IEEE International Conference on Systems, Man and Cybernetics, 'Systems Engineering in the Service of Humans'* (pp. 216–221).

7. Dauphin-Tanguy, G. (2000). *Les bond graphs*. Paris: Hermès Science Editor.
8. Deur, J., Ivanović, V., Assadian, F., Kuang, M., Tseng, E. H., & Hrovat, D. (2012). Bond graph modeling of automotive transmissions and drivelines. *Proceedings of the 7th Vienna International Conference on Mathematical Modelling (MATHMOD)*, Vienna, Austria.
9. Etienne-Vidal, P., Pietrzak-David, M., & Bonnet, F. (2008). Mixed control strategy of a doubly fed induction machine. *Electrical Engineering (Archiv fur Elektrotechnik), 90*(5), 337–346.
10. Gallo, C., Kasuba, R., Pintz, A., & Spring, J. (1986). *Design and dynamic simulation of a fixed pitch 56 kw wind turbine drive train with a continuously variable transmission*. U.S. Department of Energy Conservation and Renewable Energy Wind/Ocean Technology Division, NASA CR-179543.
11. Gawthrop, P. J. (1995). Bicausal bond graph. *Proceedings of the International Conference on Bond Graph Modeling and Simulation (ICBGM'95)* (Vol. 27, pp. 83–88).
12. Gonzáñez-Contreras, M., Rullán-Lara, J. L., Vela-Valdés, L. G., & Claudio, S. A. (2007). Modeling, simulation and fault diagnosis of the three-phase inverter using bond graph. In *IEEE International Symposium on Industrial Electronics* (pp. 130–135).
13. Guo, Y., Keller, J., & Parker, R. G. (2012). Dynamic analysis of wind turbine planetary gears using an extended harmonic balance approach. *International Conference on Noise and Vibration Engineering*, Leuven, Belgium, September 17–19, 2012.
14. Hadi, S. (1999). *Power system analysis* (pp. 26–28). New York: McGraw-Hill Editions.
15. Hansen, A. D., Sorensen, P., Iov, F., & Blaabjerg, F. (2005). Centralized power control of wind farm with doubly fed induction generators. *Renewable Energy, 31*(7), 935–951.
16. Hansen, M. O. L., Sorensen, J. N., Voutsinas, S., Sorensen, N., & Madsen, H. A. (2006). State of the art in wind turbine aerodynamics and aeroelasticity. *Progress in Aerospace Sciences, 42*, 285–330.
17. Józef, W., Jerzy, K., & Zawiśla, S. (2006). Gears and graphs. *Journal of Theoretical and Applied Mechanics, 44*(1), 139–162.
18. Karnopp, D. (1991). State functions and bond graph dynamic models for rotary, multi-winding electrical machines. *Journal of the Franklin Institute, 328*(1), 45–54.
19. Karnopp, D., Margolis, D., & Rosenberg, R. (1990). *System dynamics: A unified approach*. New York: Wiley.
20. Kubiak, P. (1996). *Analyse symbolique des systèmes physiques modélises par bond graph en comportant des éléments multiports*. Thèse Université des Sciences et Technologies de Lille, USTL. Lille France.
21. Luo, Y., & Tan, D. (2011). Dynamics modeling of planetary gear set considering meshing stiffness based on bond graph. *Procedia Engineering, 24*, 850–855.
22. Lydia, M., Immanuel Selvakumar, A., Suresh Kumar, S., & Edwin Prem Kumar, G. (2013). Advanced algorithms for wind turbine power curve modeling. *IEEE Transaction on Sustainable Energy, 4*(3), 827–835.
23. Mezghanni, D., Andoulsi, R., Mami, A., & Dauphin-Tanguy, G. (2007). Bond graph modeling of a photovoltaic system feeding an induction motor-pump. *Simulation Modeling Practice and Theory, 15*(10), 1224–1238.
24. Mikati, M., Santos, M., & Armenta, C. (2013). Electric grid dependence on the configuration of a small-scale wind and solar power hybrid system. *Renewable Energy, 57*, 587–593.
25. Miller, A., Chang, B., Issa, R., & Chen, G. (2013). Review of computer-aided numerical simulation in wind energy. *Renewable and Sustainable Energy Reviews, 25*, 122–134.
26. Morel, L., Godfroid, H., Mirzaian, A., & Kauffmann, J. (1998). Double-fed induction machine: Converter optimization and field oriented control without position sensor. *IEE Proceedings—Electric Power Applications, 145*(4), 360–368.
27. Moriarty, P. J., & Hansen, A. C. (2005). *AeroDyn theory manual*. National Renewable Energy Laboratory NREL/TP-500-36881.
28. Mukerjee, A., Karmakar, R., & Samantaray, A. K. (1999). Modeling of basic induction motors and source loading in rotor-motor systems with regenerative force field. *Simulation Practice Theory, 7*, 563–576.
29. Mukherjee, A., Karmakar, R., & Samantaray, A. K. (2000). *Modelling and simulation of engineering systems through bond graph*. New Delhi: Narosa Publishing House.

30. Ngwomo, R. F., & Scarvarda, S. (1999). Dimensioning problems in system design using bicausal bond graph. *Simulation Practice and Theory*, 577–587.
31. Ngwompo, R. F., Scavarda, S., & Thomasset, D. (1996). Inversion of linear time-invariant SISO systems modelled by bond graph. *Journal of the Franklin Institute, 333(B)*(2), 157–174.
32. Ontiveros, L. J., Mercado, P. E., & Suvire, G. O. (2010). A new model of the doubly-feed induction generator wind turbine. *IEEE/PES Transmission and Distribution Conference and Exposition: Latin America*.
33. Patel Mukund, R. (2000). *Wind and solar power systems*. Boca Raton, FL: CRC Press LLC.
34. Patiño, C., Tapia, R., Medina, A., & Fuerte, C. (2014). Wind turbine inverse control: A bond graph approach. *IEEE International Autumn Meeting on Power, Electronics and Computing (ROPEC2014)* (pp. 1–6). doi:10.1109/ROPEC.2014.7036354.
35. Peresada, S., Tilli, A., & Tonielli, A. (2004). Power control of a doubly fed induction machine via output feedback. *Control Engineering Practice, 12*(1), 41–57.
36. Ragheb, A., & Ragheb, M. (2010). Wind turbine gearbox technologies. *Proceedings of the 1st International Nuclear and Renewable Energy Conference (INREC10)*, Amman, Jordan, March 21–24, 2010.
37. Rosenberg, R. C., & Adry, A. N. (1979). Solvability of bond graph structures with loops. *IEEE Transactions on Circuits and Systems , CAS-26*(2), 130–137.
38. S. Junco. (1999). Real- and complex-power bond graph modeling of the induction motor. *Proceedings of the International Conference on Bond Graph Modeling and Simulation (ICBGM'99)*, San Francisco (Vol. 31, pp. 323–328).
39. Sahm, D. (1979). A two-axis, bond graph model of the dynamics of synchronous electrical machines. *Journal of the Franklin Institute, 308*(3), 205–218.
40. Samantaray, A. K., Dasgupta, S. S., & Bhattacharyya, R. (2010). Sommerfeld effect in rotationally symmetric planar dynamical systems. *International Journal of Engineering Science, 48*(1), 21–36.
41. Samantaray, A. K., Dasgupta, S. S., & Bhattacharyya, R. (2010). Bond graph modeling of an internally damped non-ideal flexible spinning shaft. *Journal of Dynamic Systems, Measurement, and Control*, *132*(6), 502–509.
42. Sanchez, R., Dauphin-Tanguy, G., Guillaud, X., & Colas, F. (2010). Bond graph based control of a three-phase inverter with LC filter connection to passive and active loads. *Simulation Modelling Practice and Theory, 18*, 1185–1198.
43. Sanchez, R., Guillaud, X., & Dauphin-Tanguy, G. (2012). Hybrid electrical power system modeling and management. *Simulation Modelling Practice and Theory, 25*, 190–205.
44. Sanchez, R., & Medina, A. (2014). Wind turbine model simulation: A bond graph approach. *Simulation Modelling Practice and Theory, 41*, 28–45.
45. Tapia, R., & Medina, A. (2015). Doubly-fed wind turbine generator control: A bond graph approach. *Simulation Modelling Practice and Theory, 53*, 149–166.
46. Tore, B., & Reza, K. (2011). Wind turbine modeling using the bond graph. *IEEE International Symposium on Computer-Aided Control System Design (CACSD)* (pp. 1208–1213).
47. Xu, L., & Wei, C. (1995). Torque and reactive power control of a doubly fed induction machine by position sensorless scheme. *IEEE Transactions on Industry Application, 31*(3), 636–642.
48. Younsy, R., El-Batanony, I., Tritsch, J. B., Naji, H., & Landjerit, B. (2001). Dynamic study of a wind turbine blade with horizontal axis. *European Journal of Mechanics, A. Solids, 20*, 241–252.
49. Zaimeddine, R., & Undeland, T. (2010). DTC control schemes for induction motor fed by three-level NPC-VSI using space vector modulation. *International Symposium on Power Electronics, Electrical Drives, Automation and Motion (SPEEDAM 2010)*, Pisa, Italy, June 14–16, 2010.